Summer 7-10-2019

Comparison of Hybrid Multi-dimensional Models of a Bi-Stable Load-Switched Supersonic Fluidic Oscillator Application

Lovepreet Singh Sidhu
University of Windsor

Comparison of Hybrid Multi-dimensional Models of a Bi-Stable Load-Switched Supersonic Fluidic Oscillator Application

By

Lovepreet Singh Sidhu

A Thesis
Submitted to the Faculty of Graduate Studies
through the Department of
Mechanical, Automotive and Materials Engineering
in Partial Fulfillment of the Requirements for
the Degree of Master of Applied Science
at the University of Windsor

Windsor, Ontario, Canada

2019

Comparison of Hybrid Multi-dimensional Models of a Bi-Stable Load-Switched Supersonic Fluidic Oscillator Application

By

Lovepreet Singh Sidhu

APPROVED BY:

R. Barron
Department of Mathematics and Statistics

V. Stoilov
Department of Mechanical, Automotive and Materials Engineering

G. Rankin, Advisor
Department of Mechanical, Automotive and Materials Engineering

July 10, 2019

Declaration of Originality

I hereby certify that I am the sole author of this thesis and that no part of this thesis has been published or submitted for publication.

I certify that, to the best of my knowledge, my thesis does not infringe upon anyone's copyright nor violate any proprietary rights and that any ideas, techniques, quotations, or any other material from the work of other people included in my thesis, published or otherwise, are fully acknowledged in accordance with the standard referencing practices. Furthermore, to the extent that I have included copyrighted material that surpasses the bounds of fair dealing within the meaning of the Canada Copyright Act, I certify that I have obtained a written permission from the copyright owner(s) to include such material(s) in my thesis and have included copies of such copyright clearances to my appendix.

I declare that this is a true copy of my thesis, including any final revisions, as approved by my thesis committee and the Graduate Studies office, and that this thesis has not been submitted for a higher degree to any other University or Institution.

Abstract

Fluidic oscillators are devices capable of superimposing large pressure and velocity fluctuations on the flow through a device without the necessity of having any moving parts. The lack of moving parts makes these devices superior to conventional moving-part valves in high temperature applications. The specific application of interest in the current study is the super-plastic forming (SPF) process in which large sheets of aluminum at very high temperature are formed into the desired shape by pressurizing one side inside the SPF chamber. It is known that the introduction of pressure fluctuations onto the increasing pressure in the SPF chamber reduces the chances of the metal tearing. The use of a Bi-Stable Load-Switched Supersonic Fluidic Oscillator to create the large pressure fluctuation amplitudes is ideal for this application. A numerical investigation of a Bi-Stable Load-Switched Supersonic Fluidic Oscillator is performed to understand the performance of the device under a variety of operating conditions consistent with this application. The commercial CFD code ANSYS Fluent 17.0 is used in the present work. The computational time and memory required to complete a full three-dimensional (3D) model of the device are excessive and hence simplifications are made. This research includes a comparison of the results obtained from two such simplifications. These models are used to monitor the volume average pressure and temperature changes inside the feedback tanks and exhaust chambers during the filling process. This information is used to determine the frequency and amplitude of the pressure oscillation as well as the operational conditions at which the oscillations begin and end. The numerical simulations are also validated by comparing them with experimental results.

Dedication

This study is wholeheartedly dedicated to my beloved parents, who have been my source of inspiration and I thank you for continually providing your support. Accomplishing this would hopefully make you proud of me as much as I am proud of having you as my parents.

I would also like to dedicate this work to my supervisor, Dr. Gary Rankin for his guidance, support, and patience throughout this study. I thank you for sharing your knowledge and effective teachings with me.

Acknowledgements

I would like to express my most sincere thanks to the following:

First and foremost, to my advisor, Dr. Gary Rankin, for his excellent guidance, support, patience and inspiration but above all for believing in me and giving me the opportunity to participate in this research. I am eternally grateful. Without your help, I would not have been able to successfully complete this thesis work.

This research is jointly funded by Ontario Centre of Excellence (OCE) and AEM Power systems Inc. through a VIP II research grant. I would also like to thank Mr. Eugene Ryzer and Mr. Sam Leong for so expertly guiding me through all the aspects of this research with unparalleled enthusiasm, energy and unwavering dedication.

To the entire team of Fluid Dynamics Research Institute (FDRI) at University of Windsor, especially, Mr. Sichang Xu and Mr. Chris Peirone for overseeing all facets of this work and always giving me a helping hand when needed.

Finally, I would like to extend my thanks to all faculty and staff members of the Department of Mechanical, Automotive and Materials Engineering (MAME) and Faculty of Graduate Studies.

Table of Contents

List of Figures

List of Tables

List of Abbreviations

BC	Boundary Condition
CD	Convergent-Divergent
CFD	Computational Fluid Dynamics
RANS	Reynolds-Averaged Navier-Stokes
SFO	Supersonic Fluidic Oscillator
SPF	Super-Plastic Forming
SST	Shear Stress Transport
UDF	User Defined Function

Nomenclature

A	Area
a	Speed of sound
C	Constant
C_p	Specific heat at constant pressure
C_v	Specific heat at constant volume
F	Dimensionless frequency
f	Feedback tank pressure frequency
Hz	Hertz
k	Specific heat ratio
K	Kelvin
$\dot{m}$	Mass flow rate
M	Mach number
MPa	Megapascal
n	Polytropic index
N	Number of time steps
P	Pressure
ΔP	Pressure difference
R	Gas constant
Re	Reynolds number
T	Period of the oscillation

t	Time
Δt	Period of one-time step
v	Velocity
V	Volume
2D	Two-dimensional
3D	Three-dimensional
0D	Zero-dimensional

Special characters

ρ	Fluid density
μ	Dynamic viscosity of fluid
$\mathcal{P}$	Dimensionless pressure

Subscripts

s	Supply
t	Tank
c	Chamber
fb	Feedback tank
amp	Amplitude of oscillation
b	Chamber back pressure
in	Tank or chamber inlet
max	Maximum of range
min	Minimum of range

Chapter 1 Introduction

1.1. Scope of the study

The specific application of interest in the current study is the super-plastic forming (SPF) process in which large sheets of aluminum at very high temperature are formed into the desired shape using a gas with increasing pressure in the region on one side of the aluminum inside the SPF chamber. The major advantage of this process is that it can form large and complex shapes in one-piece, and in one operation. The finished product has excellent precision and a fine surface finish [1]. The existing super-plastic forming processes must occur slowly to avoid large strain rates, and consequent cracking and tearing of the material. This makes the process uneconomical for mass manufacturing. There is some evidence in literature to suggest that the introduction of pressure fluctuations onto the increasing pressure in the SPF chamber allows the intermittent stress relief and hence, has a favorable effect on overall material formability and properties [2]. Pressure fluctuations can be created using conventional pneumatic valves. However, these devices fail at extreme temperatures due to jamming of moving parts.

Fluidic oscillators can produce large pressure pulsations with no moving parts to jam. They are devices which generate an oscillating jet with a steady flow input. The lack of moving parts and design simplicity in fluidic oscillators makes them superior to conventional moving-part valves in high temperature applications. It is known that supersonic fluidic oscillators are capable of causing higher oscillation frequencies than the fluidic oscillators with subsonic supply [3]. Therefore, in order to create the pressure fluctuations with certain amplitudes and frequencies operating under extreme conditions,

the use of a supersonic fluidic oscillators is ideal for this application. However, the design methodology and working principle are not well understood and need further research. In order to expand upon the current understanding regarding these devices, the use of computational fluid dynamics (CFD) simulation is required. The main objective of this thesis is to numerically investigate one geometrical configuration of the supersonic fluidic oscillator to understand the performance of the device under variety of operating conditions consistent with this application.

This research thesis is part of the ongoing research on the topic of supersonic fluidic oscillators at University of Windsor. Some preliminary work has been done by Xu [4], who constructed a low pressure supersonic fluidic oscillator experimental facility in order to test the feasibility of the device for this application. This device did not include the super-plastic forming (SPF) chambers. The positive results from this study motivated the design of a high-pressure supersonic fluidic oscillator experimental facility which includes the SPF chambers as well as the generation of an accurate hybrid numerical model to predict the device performance and comparison with new experimental results.

1.2. Structure of the thesis

The discussion in the introduction has provided information on the super-plastic forming process and how the efficiency of the process can be improved using supersonic fluidic oscillators. Background information on fluidic oscillators including the different types that are available and their internal working mechanisms is presented in Chapter 2. A review of the literature related to supersonic fluidic oscillators is also presented in Chapter 2, followed by the current numerical approach in Chapter 3. The results of the

numerical simulations are discussed in Chapter 4. The conclusions followed by recommendations for further research are presented in Chapter 5.

Chapter 2 Literature Review

2.1. Historical development of fluidic oscillators

Fluidic oscillators are well known for their convenience in applications of sensing, logic, timers and fluidic control systems. The earliest advancements in fluidic oscillators occurred in the 1960's and this research topic is still of interest today. In 1957, B. M. Horton of the Harry Diamond Laboratories (now the Army Research Laboratory in Adelphi, Maryland) first thought of the fluidic amplifiers when he became aware of the fact that he could divert the direction of flue gases using a small bellows [5]. Later, this lab investigated the effects of oscillator dimensions, nozzle area ratio, and splitter distance from the nozzle throat on the frequency of the oscillation. This information was used to achieve the required objective of making "flueric" temperature sensor-oscillator design a more precise and scientific process. Their published results led several major industries to apply fluidics (then called fluid amplification) to advanced control systems. The term fluidics and fluerics (combination of 'fluid' and 'logic') are used synonymously and both are appropriate descriptions of their initial application in fluid logic circuits.

2.2. Applications of fluidic oscillators

Application of fluidic logic circuits is not widespread since their speed of operation can't compete with electronics. Recently, fluidic oscillators have received renewed interest in entirely different applications. Fluidic oscillators are more extensively being used for modifying the boundary layer separation point [6]. These devices have been developed for different applications such as temperature measurement [7], flow rate measurement [8] and increasing fuel-air mixing in ejectors [9].

2.3. Advantages of the fluidic oscillators

Fluidic oscillators are devices that produce a self-sustained, stable oscillating flow at its output from a supplied steady inflow. The oscillatory motion is driven by the inherent hydrodynamic instabilities of flow within the device. This oscillatory motion of one geometrical configuration of fluidic oscillator is shown in Figure 2.1. This device is capable of superimposing large pressure and velocity fluctuations on the flow through a device without the necessity of having any moving parts. The lack of moving parts makes these devices superior to conventional moving-part valves in high temperature applications. Fluidic oscillators have a considerable number of advantages, such as a wide range of operating frequency (not limited by inertia of mechanical components in classical hydraulic or pneumatic devices), high exit jet velocities as well as robustness and fault-tolerance over a wide range of operating conditions. Oscillations with frequencies ranging from 1 to 20 kHz have been obtained with meso-scale (nozzle sizes in the range of 200 μm to 1 mm) fluidic oscillators with very low mass flow rates (of the order of 1×10^{-3} kg/s) [10]. The absence of any moving or deformable components, makes the device fairly inexpensive and there is no need of maintenance. They comprise of several flow channels and volumes of different sizes and shapes connected to achieve the desired oscillation amplitude and frequency. Further, these devices are insensitive to electromagnetic interference (EMI) and are highly tolerant to shock and vibration loads.

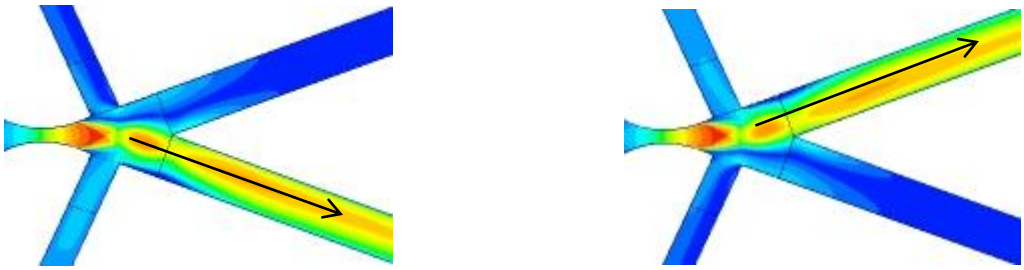

(a) (b)

Figure 2.1: Flow field of fluidic oscillator (flow from left to right) at two phase positions separated by 180^{o}

2.4. Bi-Stable Fluidic Oscillators

Based upon the various internal mechanisms that drive the oscillations, there are primarily two different types of the oscillators: (a) Feedback free fluidic oscillator (b) Feedback fluidic oscillator. Feedback free oscillators, also referred to as jet-interaction fluidic oscillators are based on the inherent fluid dynamic instabilities from the incoming jet. When this jet flow interacts within the cavity it leads to an oscillatory jet flow at the output of the chamber [11]. Feedback fluidic oscillators will be described in detail since they are the main focus of this thesis. Many other types of fluidic oscillator can be found in the literature with different geometries consistent with different applications [12].

2.4.1. Wall-attachment fluidic oscillators

A wall-attachment fluidic oscillator consists of a supply port that provides mass flow to the oscillator, output ports which connect the pulsating flow to the desired output device and control ports which can be used to provide feedback flow. The classical wall-attachment fluidic oscillator is shown in Figure 2.2.

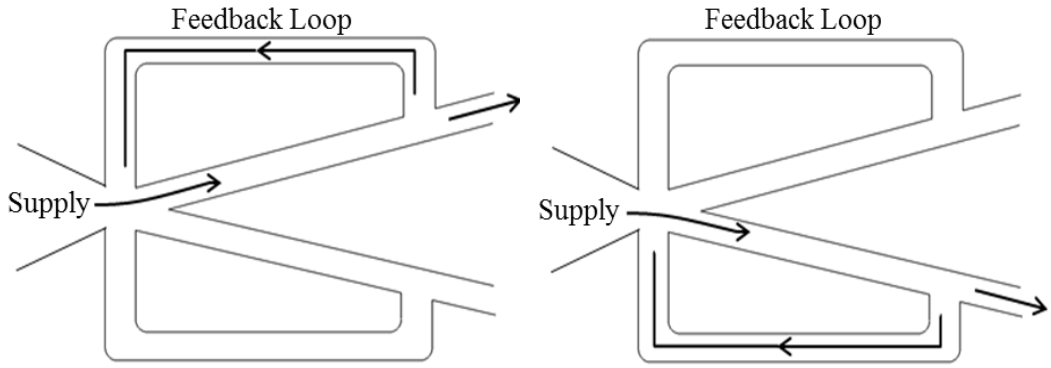

Figure 2.2: A wall-attachment fluidic oscillator with feedback loop

The supply jet flow through the main nozzle attaches to one of the two side walls inside the device. The primary physical phenomenon responsible for attachment of the jet to the adjacent wall is the Coanda effect. A mixing region is formed between the main jet flow and the adjacent wall as indicated in Figure 2.3. The velocity of fluid in this region is much slower than the main jet and includes flow reversal. As the flow passes through this region, a part of the surrounding fluid will be entrained with the main flow and accelerated along with the flow. This leads to a local reduction of pressure in the mixing region.

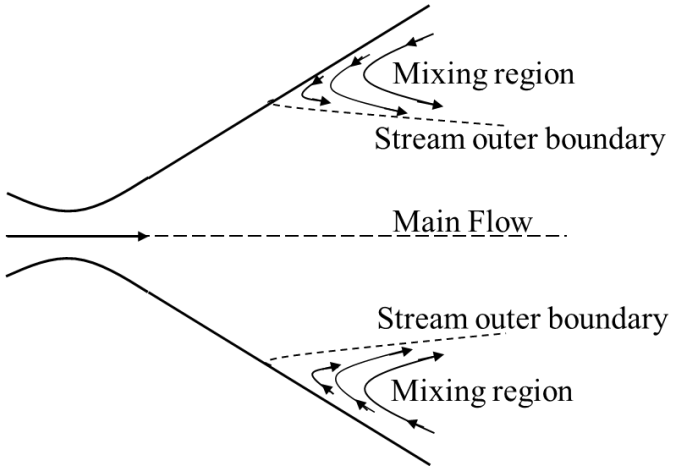

Figure 2.3: Supersonic main flow with separation and entrainment from immediate surroundings

Due to any disturbances in the flow, the entrainment process will be stronger on one side than the other. This difference leads to a transverse pressure gradient across the supersonic jet with a lower pressure on the side with less entrainment. As a result, jet will deflect to the side with lower pressure. As the jet moves closer to the wall, entrainment is further restricted, the pressure drops further, and jet deflection is increased until the jet is attached to the wall as shown in Figure 2.4. The jet will remain attached to the adjacent wall as long as there is not an adverse pressure gradient along the wall sufficiently strong to induce separation [13].

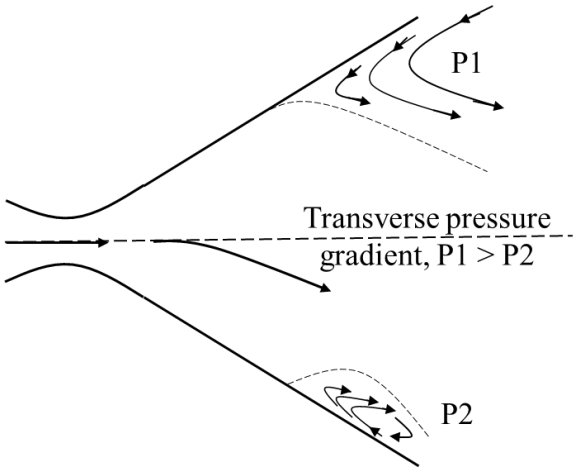

Figure 2.4: Flow reattachment due to Coanda effect

The instantaneous pressure distribution is lower on that wall due to the lack of jet entrainment on that side. Disturbances in the downstream flow are transmitted back to the point of the jet separation in the supply nozzle through the feedback channel and control port (the exact source of this disturbance and its path depends on the sub-type of wall-attachment oscillator). This creates a transverse pressure difference which ultimately causes the jet to deflect to the opposite side wall of the device. This process completes a half-cycle of the oscillation. Due to the geometrical symmetry, the same phenomenon

occurs on the other side of the device and the jet oscillates between the two side walls in a periodic manner.

The side, to which flow attaches initially, is governed by the geometry of the oscillator and disturbances introduced in the flow. If the oscillator is geometrically symmetrical, the initial jet attachment is solely governed by naturally introduced asymmetries in the flow. The fact that the flow can attach equally to either of two walls makes the oscillator Bi-Stable.

The feedback loop is important to continually cause switching from one channel to the other and maintain the oscillation. The feedback path however, need not have the geometrical configuration shown in Figure 2.2. Based on different feedback path configurations, different sub-categories of wall-attachment fluidic oscillator can be defined: the 'sonic oscillator', the 'relaxation oscillator', and the 'load oscillator' [12,14].

(A) Sonic oscillator

In the sonic oscillators, feedback path is achieved by interconnecting the control ports (Figure 2.5). When the flow attaches to one side, air from the control channel on that side is also entrained with the main flow and creates an expansion pressure wave. This expansion wave propagates through the interconnection tube to the control channel on the other side. Simultaneously, an increase in pressure on other side produces a compression wave in the interconnection tube. When the disturbances propagate through the tube and reach the control ports on the opposite side, the jet switches and attaches to the wall on the other side [12]. This type of the oscillator is called a sonic oscillator. The period of oscillation is inversely proportional to the speed of wave propagation of the fluid in the feedback loop.

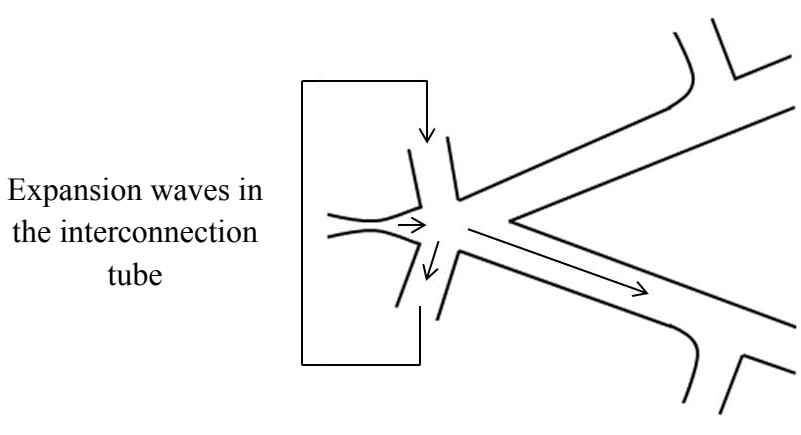

Figure 2.5: Sonic oscillator

(B) Relaxation oscillator

The relaxation oscillator allows part of the output flow to be fed back to the jet attachment region through the feedback channel to the control ports as indicated in Figure 2.6. The resulting pressure waves and the returned mass flow momentum cause the jet to switch to the other side. The dimensions, location and orientation of the feedback loop are important parameters in determining the performance of the relaxation oscillator [15].

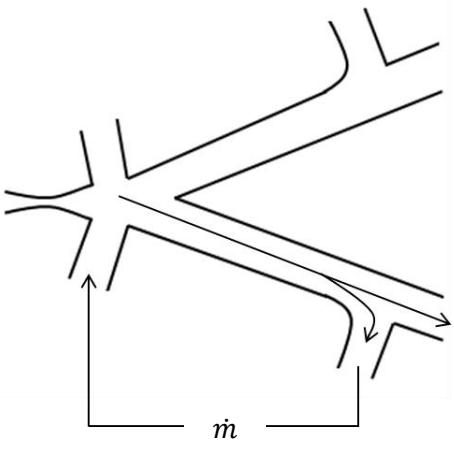

Figure 2.6: Relaxation oscillator

(C) Load oscillator

In this case the feedback path is through the output channel itself. This effect is achieved by adding a resistance or load in the downstream region which leads to the local increase in pressure that opposes the main flow and propagates upstream as shown schematically in Figure 2.7. This increase in pressure on one side of the supply jet causes it to switch to the other side. Once the flow attaches to either attachment wall, it remains attached until the downstream pressure builds up to certain level, such that it restricts the flow and switches it to the other side of the oscillator. After the switch, the built-up downstream pressure dissipates, and the same process occurs on the opposite side of the oscillator [16]. For the load oscillator, the rate of compression of the fluid in the load chambers determines the amplitude and frequency of the oscillation. Fluidic micro-bubble generators are based on the load switching mechanism [14], where each output channel of the oscillator is tangentially connected to a vortex chamber. The downstream pressure increases due to the vortex being formed in the chamber attached to that output and this pressure build up forces the main oscillator flow jet to switch to the other side of the oscillator.

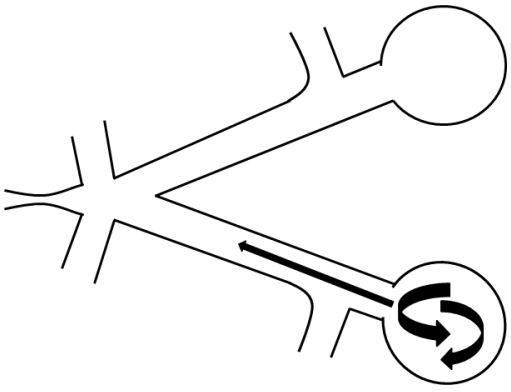

Figure 2.7: Load oscillator

2.5. Fundamental fluid dynamics

This section gives a brief introduction to the fundamental fluid dynamic principles that are used in Bi-Stable Load-Switched Supersonic Fluidic Oscillators.

2.5.1. Convergent-Divergent nozzle

A convergent-divergent, or CD, nozzle is just a specially shaped tube with fixed convergent section followed by a fixed divergent section, shown in Figure 2.8. In a CD nozzle, the gas flows from the high-pressure chamber (usually this chamber is large enough so that any flow velocities there are negligible) and converges down to the minimum area, or throat**,** of the nozzle. The flow is choked at the throat which sets the mass flow rate through the system. Downstream of the throat, the geometry diverges, and the flow is isentropically expanded to a supersonic Mach number that depends on the area ratio of the exit to the throat and the downstream pressure in the ideal design condition.

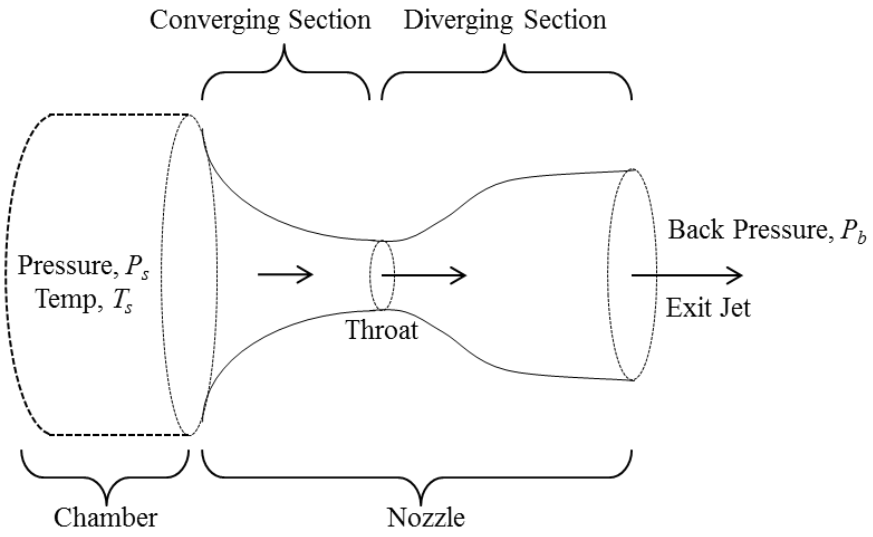

Figure 2.8: Converging-diverging nozzle configuration

The expansion of a supersonic flow causes the static pressure and temperature to decrease from the throat to the exit, so the amount of the expansion also determines the exit pressure and temperature and hence exit speed of sound and velocity. The following derivation is used to explain why a supersonic flow accelerates in the divergent section of the nozzle while a subsonic flow decelerates in a divergent duct.

From conservation of mass equation;

$$\dot{m} = \rho v A = Constant$$

$$\frac{d\rho}{\rho} + \frac{dv}{v} + \frac{dA}{A} = 0 \tag{1}$$

From the momentum equation under these conditions;

$$\rho v \, dv = -dp \tag{2}$$

For isentropic flow,

$$\frac{dp}{p} = k \frac{d\rho}{\rho}$$

$$dp = a^2 d\rho \tag{3}$$

Combining the isentropic flow equation with mass conservation and momentum equation and using the definition of Mach number, $M = v/a$, we get;

$$(1 - M^2) \frac{dv}{v} = -\frac{dA}{A} \tag{4}$$

This equation indicates how the velocity, v changes when the area, A changes, and the results depend on the Mach number, M of the flow. If the flow is subsonic ($M < 1$), the increase in area decreases the velocity. For a supersonic flow ($M > 1$) the increase in area increases the velocity. This effect is exactly the opposite of what happens subsonically. This is a result of the fact that conservation of mass in a supersonic (compressible) flow involves both a change in the density and the velocity as the area changes.

2.5.2. Flow pattern in the divergent region

The subsonic flow, when accelerated to supersonic speed through a convergent-divergent nozzle, must first reach a Mach number of one at the nozzle throat (choking). The mass flow rate through the nozzle is now fixed for constant supply conditions. For the isentropic inviscid flow, the mass flow can be calculated using Equation 5 [17].

$$\dot{m} = \frac{A\,P_t}{\sqrt{T_t}} \sqrt{\frac{k}{R}} \left(1 + \frac{k-1}{2}\right)^{-\frac{k+1}{2(k-1)}} \tag{5}$$

Also, once the flow is choked, the pressure distribution in the converging section cannot change with changes in the back pressure. Depending upon the back pressure condition, different flow regimes are observed in the divergent section of the nozzle.

(a) Over expanded flow: As the back pressure is lowered below that needed to choke the flow, a region of supersonic flow forms just downstream of the throat. Unlike a subsonic flow, the supersonic flow accelerates as the area gets larger. With certain back pressure conditions this region of isentropic supersonic acceleration can contain a normal shock wave. The flow downstream of the shock stays attached to the wall, as shown in Figure 2.9. The shock wave produces a near-instantaneous deceleration of the flow to subsonic speed. This subsonic flow then decelerates through the remainder of the diverging section and exhausts as a subsonic jet. The length of supersonic flow in the diverging section before the shock wave is increased by reducing the back pressure to the point where it is at the exit. A further lowering of the back pressure causes the normal shock to exit the diverging section and form an oblique shock wave outside of the nozzle.

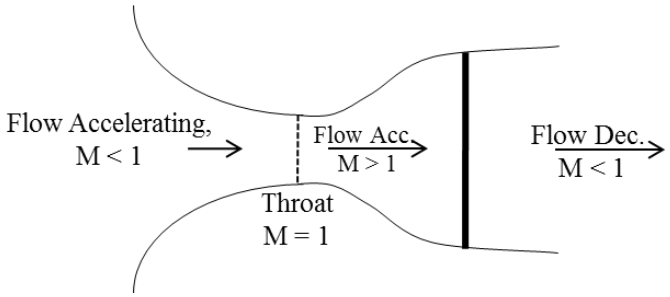

Figure 2.9: Over expanded flow pattern in converging-diverging nozzle

(b) Perfectly expanded flow: Eventually the back pressure is lowered enough so that it is now equal to the pressure at the nozzle exit. In this case, the oblique shock wave in the jet disappears altogether (Figure 2.10), and the jet will be uniformly isentropic and supersonic. Since this condition is desirable, it is referred to as the 'design condition' or perfectly expanded.

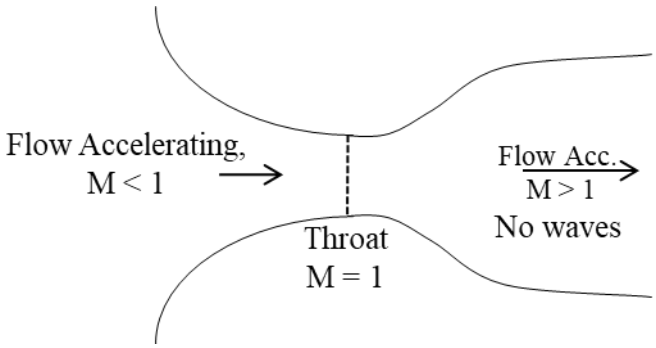

Figure 2.10: Perfectly expanded flow pattern in converging-diverging nozzle

(c) Under expanded flow: If the back pressure is lowered even further, it will create a new imbalance between the exit and back pressures (exit pressure greater than back pressure, Figure 2.11). In this case, the flow continues to expand outward after it has exited the nozzle. Expansion waves are formed at the nozzle exit, initially turning the flow at the jet edges outward in a plume and setting up a different type of complex wave pattern.

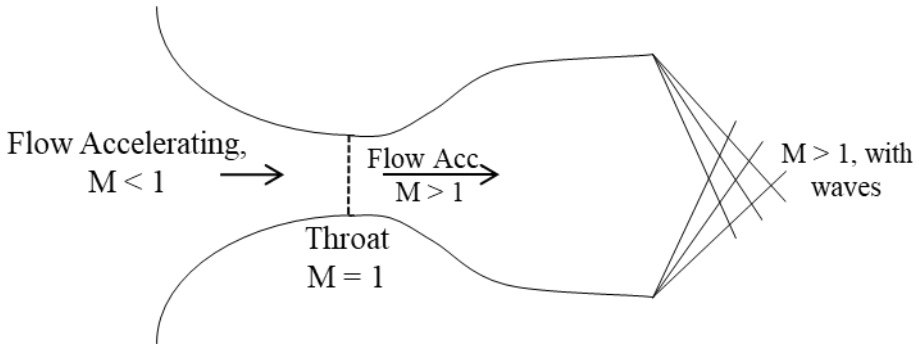

Figure 2.11: Under expanded flow pattern in converging-diverging nozzle

In real flows, viscous effects like the wall boundary layer and flow separation drastically alter the flow pattern in a CD nozzle. The flow separation leads to the formation of complicated oblique (Lambda) shocks as a consequence which is shown in Figure 2.12. Flow downstream of the shock is non-uniform and its structure is also very complex [18].

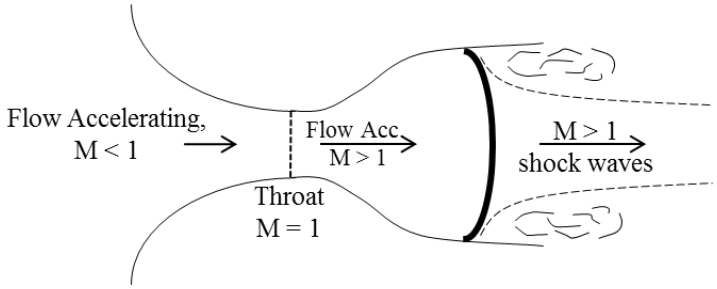

Figure 2.12: Shock structure and flow pattern in converging-diverging nozzle for viscous (separated) flow

2.6. Literature review of supersonic fluidic oscillators

Several investigators have studied the fluid flow mechanisms for subsonic and supersonic fluidic oscillators and it has been found that the frequency and amplitude of the self-induced oscillations can increase linearly with the increasing Mach number [3]. In the current chamber pressurization application, large pressure pulsations are required and

hence, supersonic fluidic oscillators are most desirable however they are more difficult to understand. There are several investigations with supersonic fluidic oscillators that serve as a basis for further work in this area.

2.6.1. Geometrical design of the oscillator

Thompson [19] conducted an experimental study regarding a supersonic Bi-Stable switch and provide some crucial empirical design data for optimum performance of the device. For visual interpretation of flow field, the Schlieren method was used as the flow visualization technique. The dynamic characteristics of the Bi-Stable Supersonic Fluidic Amplifier were experimentally studied. The locations of the flow separation and reattachment points were measured for different back pressure conditions, holding the supply pressure constant at three different constant values. It was found that that separation begins at a particular pressure ratio, i.e. the ratio of the minimum pressure prior to separation to that immediately after was virtually constant for any assumed flow situation. The position of minimum pressure (i.e. $dP/dx = 0$) prior to separation was seen to increase with increase in supply pressure and throat area but decrease with increase in wall angle and back pressure. With a constant supply pressure, increasing the back pressure decreases the size of the vortex region and moves the vortex region upstream.

Thompson later extended his work to determine the optimum design parameters for the supersonic fluidic oscillator and experimentally studied the effect of the geometrical design on the performance of the device [20]. Control port position and width were adjusted, and its effects on jet attachment stability were determined. The other adjustable design parameters for the study were the divergent angle, the divergent wall length and the splitter position. A limiting value of control port width (2.16 mm) was determined and it

was concluded that to ensure effective switching at all operating conditions; control port width should not be less than 2.16 mm. The divergence angles studied included values of 30, 40 and 50^{o} respectively, and it was found that increasing the divergent angle increases the effective working range of the amplifier for any given position of control port. From these results, it was concluded that the 40^{o} divergent angle provides the most stable operation. The length of the divergent walls should be long enough to permit the vortex region to form on the walls, which means that the wall length should be greater than the position of the flow reattachment. The experimental result showed that the minimum wall length should exceed the reattachment distance by 20%. The ideal position of the splitter occurs when there is minimum interference between the tip of the splitter and the main flow jet. The outer streamline of the jet separating on the free wall may then be assumed to be parallel to the opposite (reattached) wall. The tip of the splitter was suggested to be placed at a center line point close to the horizontal distance of the flow reattachment.

Raghu [10] studied the small scale (nozzle sizes in the range of 200 μm – 1 mm) Bi-Stable Fluidic Oscillators to understand the mechanism by which flow control was achieved by these sweeping jets. In his study, he used a feedback-type fluidic oscillator where the momentum of the flow emerging from the feedback channel was used as the switching mechanism. Raghu summarized the effects on the device performance with the transition from macro to micro-scale fluidic devices. The four different scales are discussed and are referred to as “macro” (10 cm), “sub-scale” (1 cm), “miniature” (1 mm) and “micro” (100 microns) [21]. The “macro” scaled fluidic nozzle provided the oscillation frequencies less than 300 Hz even at very high flow speeds. Fluidic excitations were at 170 Hz for the “sub-scaled” fluidic oscillator. Frequencies higher than 2000 Hz were easily

achieved with the “miniature” scaled fluidic oscillator and the mass flow rates were extremely small in this case. “Micro” fluidic nozzles with the dimensions of the order of 100 microns could produce oscillation frequencies over 10 kHz. They concluded that the frequency of oscillation depends on the length and volume of the feedback loop. By adjusting the geometry of the wall-attachment region in the cavity and the length of the feedback channels, the time spent by the jet at the extreme positions and the switching method of the jet can be varied. This results in a variety of wave shapes, for example, sine, saw tooth and rectangular waveforms.

2.6.2. Review of numerical studies of the supersonic Bi-Stable Fluidic Oscillator

Gokoglu conducted an analysis of the internal flow structure and performance of a fluidic diverter actuator over the range of low subsonic to sonic inlet conditions using time-dependent numerical computations, and also extended his work for supersonic flows [3]. The numerical investigation was done using the commercial CFD software FLUENT 6. The computational domain was two-dimensional (2–D). The supply pressure at the inlet of the converging nozzle was maintained at different constant pressure values and a temperature of 298 K while the actuator opens to the ambient environment at 1 atm and 298 K at the two outlets. The walls were assumed to be at constant ambient temperature of 298 K. This study includes cases with supply-to-ambient pressure ratios up to 17.1 and Mach numbers up to 2.5.

He compared the numerical predictions with his own experimental measurements and found excellent agreement for the calculated oscillation frequencies with respect to flow rate. The frequency of the oscillation increases linearly with the flow rate. The delay time for the initiation of the steady, periodic oscillations decreases with the flow rate for

subsonic flows and levels off at a minimum when the Mach number exceeds unity. The working fluid was also varied (air versus helium) and it was observed that oscillation frequencies for helium at a given Mach number were larger than those for air due to the higher sonic speed. Two different switching mechanisms were also observed as the Mach number was increased. The transition from the complete-switching "flip-flop" mode, where the flow occupies only one outlet before switching direction, to the partial switching "spill-over" mode, where the flow shifts only partially between the outlet channels, was also discussed. This transition depends on the internal geometrical parameters such as the length of the feedback channels.

Xu [22] also developed a simple hybrid numerical model for the supersonic fluidic oscillator as shown in Figure 2.13. This design considered the load-switching mechanism as described below.

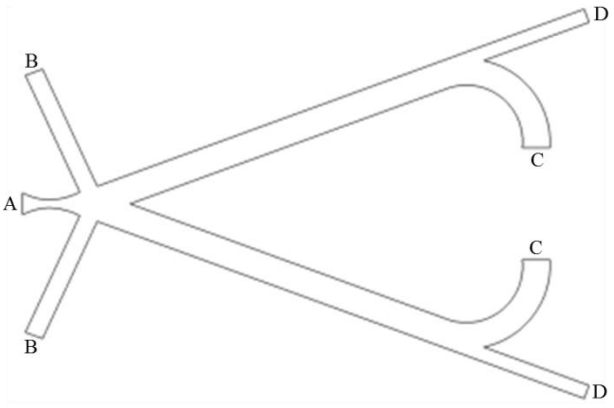

Figure 2.13: Xu's supersonic oscillator model geometry with boundary conditions

The labels A, B, C and D in the diagram above represent the supply inlet, control port inlets, outlets to the atmosphere and connection to the feedback tanks respectively. The supply inlet (A) connects a supply of high pressure compressed air to the inlet of a

converging-diverging nozzle to produce the supersonic jet. This jet then enters a chamber with control channels (B) on either side as well as two diverging outlet channels separated by a flow splitter situated downstream and directly in front of the nozzle. Each feedback channel has a feedback tank (D) attached to it, located before the outlet to the atmosphere (C). Under certain back pressure conditions, the jet oscillates between the two outlets due to the alternate pressure build up (load) in each feedback tank. This device was based on Hiroki's high-power Bi-Stable Supersonic Fluidic Oscillator designed for use in a fatigue testing machine [21]. The oscillating output jets (C) were used to impact the test piece to produce vibrations in the solid structure with a certain amplitude and frequency.

Xu studied the effect of feedback tank volume, supply pressure, control port resistance and outlet back pressure on the oscillation frequency and the amplitude of the feedback tank pressure fluctuation. The frequency decreases with increase in feedback tank volume and gives good agreement in trend with Hiroki's experiment. Xu also developed an in-house experimental facility to validate his numerical model because of the lack of detail in description of Hiroki's experimental operating conditions [4]. It was concluded that a stable oscillation only occurs within a range of supply pressure, provided the exhaust chamber pressure and control channel resistance remain constant. The dimensionless oscillation frequency and dimensionless feedback tank pressure amplitude have the same trend as the experimental results in this range of stable oscillation. For a constant supply pressure, increasing control port resistance decreases the dimensionless frequency and increases the dimensionless feedback tank pressure amplitude. Increases in the back pressure cause the dimensionless feedback tank amplitude to increase but do not have

significant effect on the dimensionless oscillation frequency over the range of back pressures considered.

There is a problem with the Xu's (Hiroki's) oscillator design for the SPF application. As the chamber pressure or back pressure is increased, a value is reached where flow exits the control ports rather than entering the chamber. Two methods of overcoming this problem have been investigated; 1) connecting each control port to its respective feedback tank and 2) connecting both control ports to the SPF chamber. It is found that connecting both control ports to the SPF chamber yields a higher amplitude of pressure oscillation (Figure 2.14). The results show that having separate SPF chambers gives larger oscillation pressure amplitudes [24]. Hence, further research is conducted with that configuration.

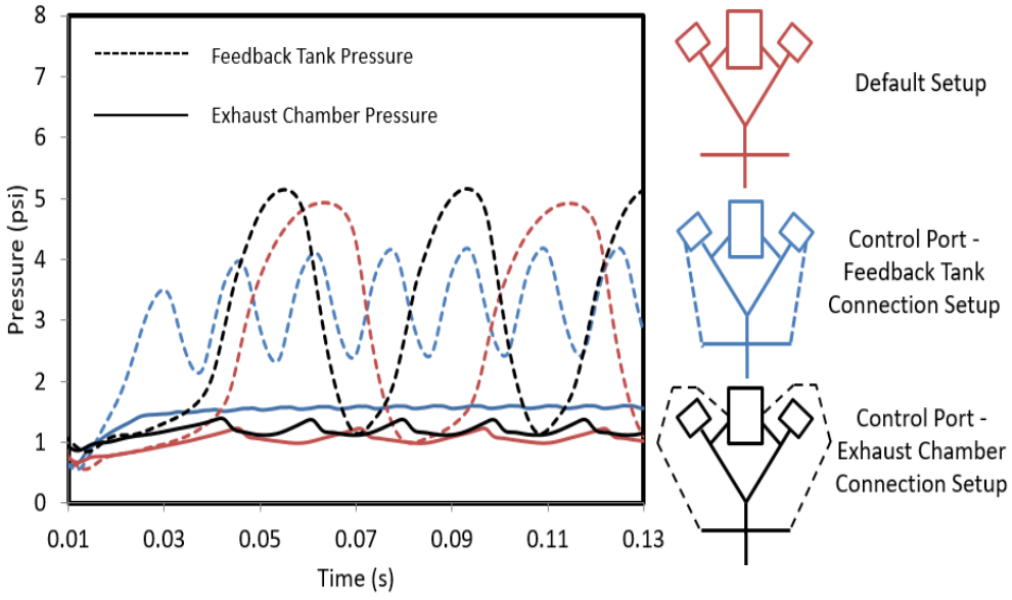

Figure 2.14: Pressure amplitude versus time for different oscillator configurations

In the current research, Xu's numerical model is modified and further refined to be consistent with the chamber pressurization application. In order to validate the numerical model, a study is being conducted simultaneously, by another graduate student (Mr. Chris Peirone) using an in-house, high-pressure, experimental facility located in the Jet/Vortex Lab at the University of Windsor's Centre for Engineering Innovation.

2.7. Objectives of the current research

As mentioned earlier in the introduction, the main objective of this thesis is to numerically investigate a Bi-Stable Load-Switched Supersonic Fluidic Oscillator and understand the performance of the device under a variety of operating conditions consistent with super-plastic forming application. For this purpose, two different numerical approaches are taken:

1. A two-dimensional (2D) CFD model of the flow in the oscillator channels combined with a zero-dimensional (0D) model for the feedback tanks and the super-plastic forming chambers.
2. A two-dimensional (2D) CFD model of the flow in the oscillator channels combined with a three-dimensional (3D) model for the feedback tanks and the super-plastic forming chambers.

The fundamental objective is additionally broken into the following sub-objectives:

- Develop an accurate numerical model of the Bi-Stable Load-Switched Supersonic Fluidic Oscillator best suited for the application and provide important design information for construction of the experimental facility.

- Investigate the internal flow phenomena which occur in a Bi-Stable Load-Switched Supersonic Fluidic Oscillator during an oscillation cycle.
- Investigate the given geometrical design to find out the frequency and the amplitudes of the oscillation.
- Determine the conditions for stable oscillation as well as the stable oscillation range.
- Make a qualitative and quantitative comparison of the experimental and numerically simulated flow field characteristics.
- Make a comparison of the performance characteristics for different sizes of the oscillator.
- Make a comparison of the computational load and capability of the 2D-0D and 2D-3D hybrid models.

Chapter 3 Numerical Model Setup

The numerical investigation is performed using the commercial computational fluid dynamics (CFD) software, ANSYS Fluent 17.0. This chapter gives a description of the geometry, meshing, flow assumptions, boundary and initial conditions and numerical solution schemes used in this CFD model. The computational time and memory required to complete a full three-dimensional (3D) model of the device are excessive and hence simplifications are made. The first simplification is a combination of a two-dimensional (2D) CFD solution of the flow in the oscillator channels and a zero-dimensional (0D) model for the feedback tanks and the super-plastic forming chambers. The second simplification utilizes the same 2D CFD model as in the first simplification but replaces the 0D model with three-dimensional (3D) CFD solutions.

There is no established design methodology for the design of the fluidic oscillators. These actuators come in various forms and shapes and a detailed study is complicated by the proprietary nature of such designs. The frequency of the fluidic oscillator is generally determined by its geometry and the supply pressure (flow rate). In the current study, the geometrical dimensions are taken from Xu's experiment [4] and the oscillator is scaled down by the factor of 3 to be consistent with a laboratory prototype constructed for further experimentation. The final design of the flow channels within the oscillator along with the dimensions (in millimeters) are shown in Figure 3.1. The thickness of the oscillator perpendicular to the paper is 3.2 mm.

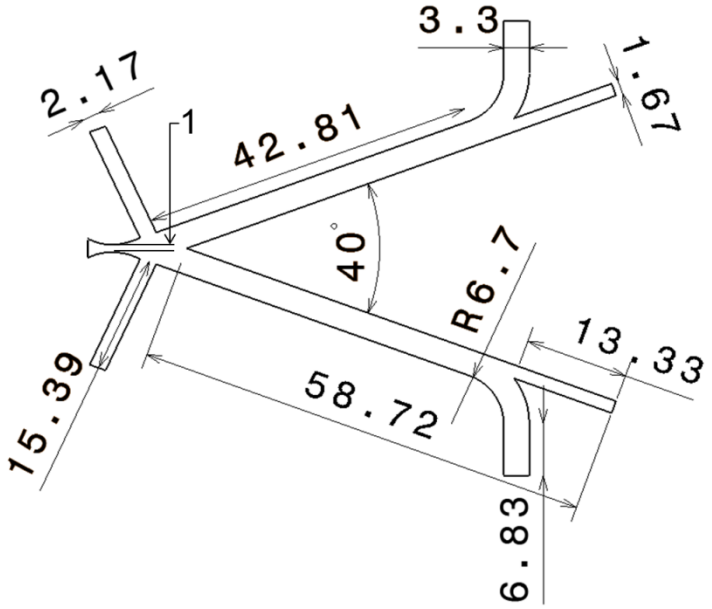

Figure 3.1: Design of the flow channels in oscillator (dimensions are in millimeters)

The converging-diverging nozzle is connected to the supply reservoir on the left which is large enough to reduce any flow disturbances and provide a steady flow to the device. The control channels and the branch of output channels curving outwards on either side of the oscillator are connected to the super-plastic forming chambers as shown schematically in Figure 3.2. The other branch which is parallel to the output channels is connected to the feedback tanks to create a time varying resistance to the flow downstream which is responsible for the oscillation.

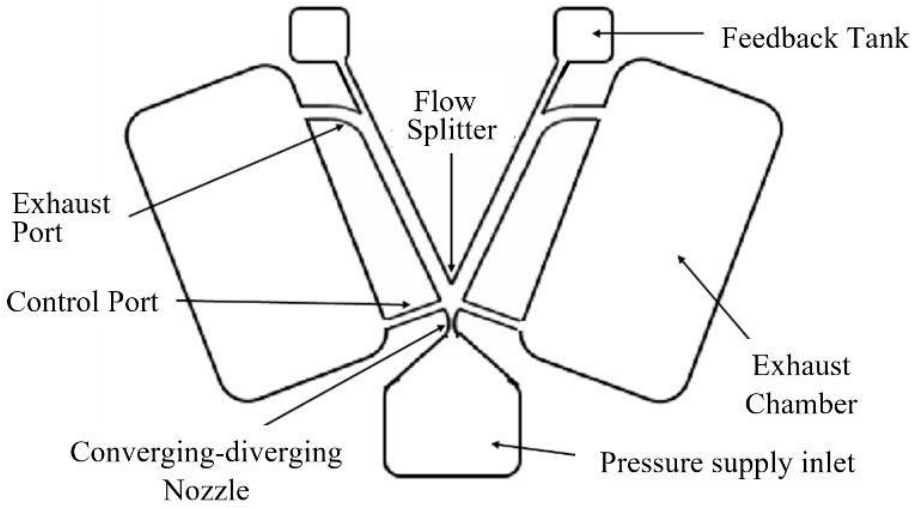

Figure 3.2: Schematic of the Bi-Stable Load-Switched Supersonic Fluidic Oscillator configuration with control port and exhaust port connection. Note: This figure is not to the scale

3.1. Description of the 2D/0D numerical model

This hybrid model is a combination of a two-dimensional (2D) CFD solution of the flow in the channels and a zero-dimensional (0D) model for the feedback tanks and the exhaust chambers shown schematically in Figure 3.3. The 0D models are sometimes referred to as lumped parameter models and based on the assumption that the flow variables such as pressure and temperature are uniform throughout the region being modeled while ensuring that the appropriate integral equations of fluid motion are satisfied.

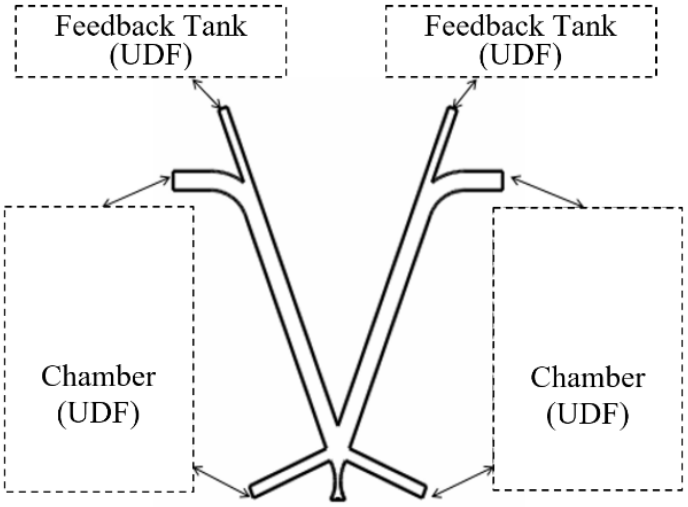

Figure 3.3: 2D/0D model of the supersonic fluidic oscillator

The 0D models are easily implemented as boundary conditions using the User Defined Function (UDF) capability of ANSYS Fluent. The UDF for the 0D model is given in the Appendix B.1. The UDF requires use of monitored values of the mass flow rates and mass-weighted static pressures at locations in the flow field just outside the feedback tanks and exhaust chambers. Equation (6) [4], which assumes a polytropic thermodynamic process in the tank, is used along with these monitored values to determine the pressure inside feedback tanks and exhaust chambers. The polytropic index "n" in this equation is 1.4 for an isentropic process and 1 for an isothermal process.

$$\frac{d}{dt}\left(P_{t/c}\right) = \left[n * R * \left(T_{t/c}\right)_{in} * \left(\dot{m}_{t/c}\right)_{in}\right] / V_{t/c} \tag{6}$$

The feedback tanks are simulated using lumped parameter models for the tank filling and discharging process using the isentropic/isothermal assumption. The UDF compares the pressure inside the tank with the pressure in the region just outside the tank inlet. If the total pressure outside is larger than the tank pressure, flow is allowed to fill the feedback tank; otherwise, the feedback tank is full or discharging. For either the charging

or discharging process, once the downstream to upstream total pressure ratio is lower than the choking criteria which is 0.528 for an ideal gas, the flow is assumed to be choked at the tank inlet.

The SPF chambers are also simulated using a similar lumped parameter model as for the feedback tanks. The only difference is that SPF chambers have two inlets, control port inlet and exhaust port inlet, instead of having one inlet in case of feedback tanks. At the end of each time step, the pressure change in the feedback tanks and SPF chambers is determined using the mass flow rate through the inlet at that instance of time as calculated from the CFD solution for flow inside the channels. The lumped parameter (0D) models for both the feedback tanks and SPF chambers are discussed in more detail in the Appendix A.

3.2. Computational mesh

The mesh for this geometry is generated in ANSYS Meshing. The numerical mesh is formed by splitting the flow geometry into sections to allow better control over mesh sizes as shown in Figure 3.4. Any two adjacent sections still remain connected at the split point, but now the dimensions and position of each section can be manipulated independently.

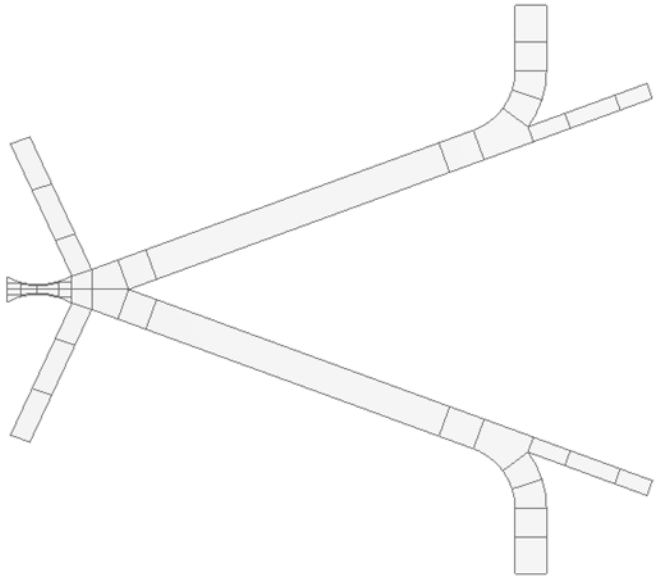

Figure 3.4: Oscillator geometry with split faces

A structured quadrilateral mesh is generated and the sensitivity of the solution to grid size is investigated. Grid auto adaptation is also employed based on the local pressure gradients, every 25 time steps. The solution-adaptive mesh refinement feature of ANSYS Fluent allows you to refine and/or coarsen the mesh based on geometric and numerical solution data [25]. It is assumed that the greatest error in the solution occurs in high pressure gradient regions, therefore, the readily available physical features of the evolving flow field are used to drive the grid adaption process. This helps to accurately locate the shocks and resolve the pressure amplitudes. An example of this refinement is indicated in Figure 3.5.

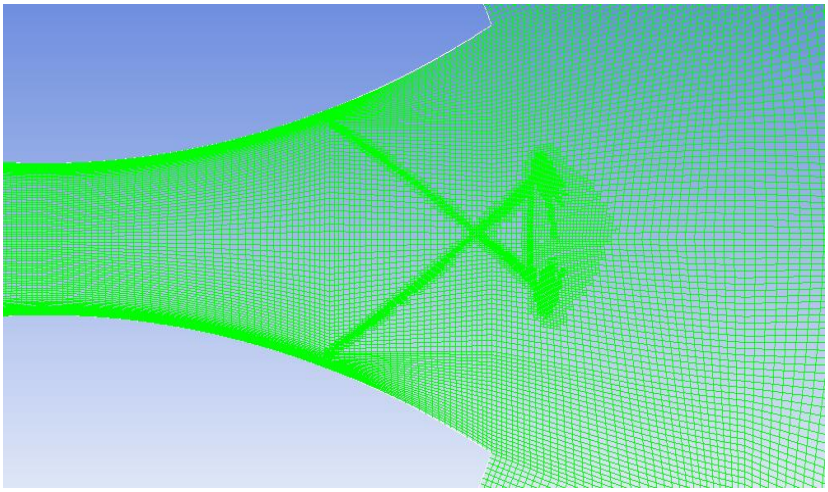

Figure 3.5: Solution-adaptive mesh refinement based on the pressure gradient

In order to determine the influence of the spatial mesh resolution, a grid study is carried out with three different grids. Three grids (denoted as "Coarse", "Intermediate", and "Fine") are used to estimate the mesh sensitivity. The coarse grid has 33000 elements, intermediate grid has 62000 elements and fine grid has 124000 elements (approximately). Preliminary calculations are made to compare the results obtained with these grids. The control port pressure is monitored and used as the measure to determine changes due to grid size, as the pressure fluctuations are most sensitive at this location. The computational results over one cycle, for the intermediate and fine meshes are plotted in Figure 3.6. The refined mesh gives a relative change in the average value of the control port pressure difference of only 0.99% over one cycle and a relative frequency difference of only 1.23%. The intermediate grid resolution with 62539 computational cells is considered to be within an acceptable error hence, all subsequent simulation work is performed with the intermediate mesh.

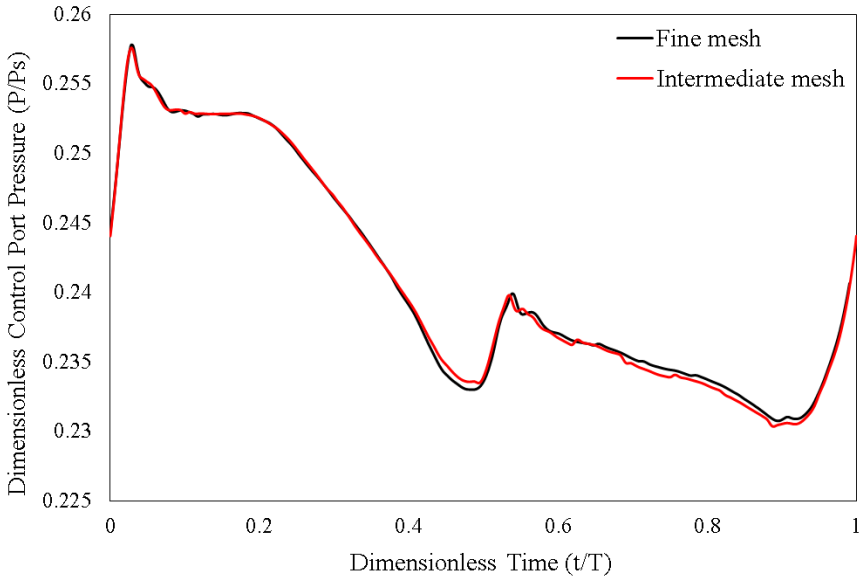

Figure 3.6: Dimensionless control port pressure versus dimensionless time for mesh sensitivity study

The time step independence study with fixed time step sizes is conducted to ensure a high temporal resolution of the jet oscillation. Three different time step sizes (denoted as "Coarse", "Intermediate", and "Fine") are used to estimate the time step sensitivity. The coarse time step is 1×10^{-3} seconds, intermediate time step is 1×10^{-4} seconds, and fine time step is 1×10^{-5} seconds. A time step independence study indicates that a time step of 1×10^{-3} seconds gives a 2.52% difference in control port pressure and frequency difference of 2.2% compared to a time step size of 1×10^{-4} seconds. Whereas, a time step of 1×10^{-4} seconds gives 0.93% difference in control port pressure and frequency difference of 1.2% compared to a time step size of 1×10^{-5} seconds. Therefore, a time step size of 10^{-4} seconds is used in this study. The computational results, over one cycle, for dimensionless control port pressure versus dimensionless time are plotted for intermediate and fine mesh in Figure 3.7.

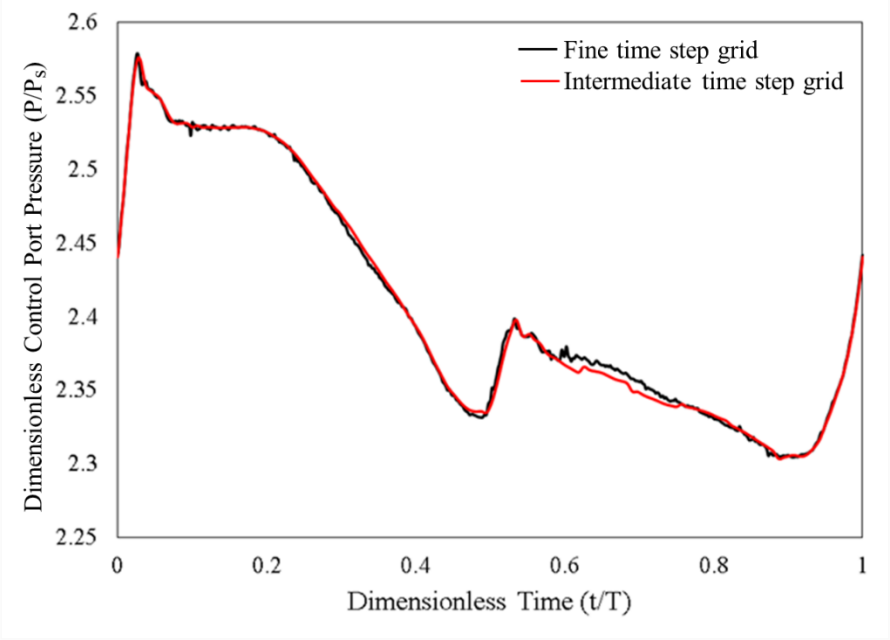

Figure 3.7: Dimensionless control port pressure versus dimensionless time for time step sensitivity study

3.3. Boundary conditions for numerical simulations

The converging-diverging nozzle is connected to the reservoir (not included in the solution domain) which provides the constant supply pressure and this value is set equal to the reservoir pressure value. All the connections from the flow channels to the SPF chambers and feedback tanks are assumed to be pressure inlets. The pressure inlet boundary condition in Fluent provides more control over the flow properties [25]. The control ports and the exhaust ports are connected to flow channels on either side and are set as pressure inlets at pressure values calculated based on the pressure change inside the SPF chambers. A porous jump boundary is located in each of the control channels to allow a setting of the channel resistance in the form of a constant minor loss coefficient. The minor loss coefficient is estimated to be 0.75 which is consistent with the minor loss for a

90-degree elbow and chamber entrance. The walls in the model are assumed to be adiabatic walls with the no slip condition imposed. The wall roughness for the solid walls in the model is taken to be 0.0032 mm which is standard for a machined aluminum surface. Either air or nitrogen with ideal gas properties are used as the flow medium to determine its effect.

3.4. Numerical solution

The governing equations are solved using the double-precision density-based implicit Algebraic Multigrid (AMG) solver for each cell. For high-speed compressible flows, the density-based solver is the preferred option because it includes the energy equation in the coupled system, resulting in a single matrix equation to be solved. For the cases considered in this thesis, the Reynolds number is large enough to assume fully turbulent flow and neglect laminar-to-turbulent transition effects. The k-omega SST turbulence model is utilized in the calculation as it offers a more accurate treatment of the near-wall region than the k-ε turbulence model and is reliable for flows with adverse pressure gradients. The second order upwind schemes are chosen for spatial discretization. Second order upwind scheme is used for discretization of convective terms and central differencing scheme is used for discretization of diffusion terms in the transport equation. Second order implicit schemes are used for transient formulation. The second-order upwind scheme provides stability for supersonic flows and captures shocks better than the first-order upwind scheme; the tradeoff is in the time to convergence [3].

3.5. Description of the 2D/3D numerical model

This hybrid model utilizes the same 2D CFD model as in the first simplification but replaces the 0D models with separate three-dimensional (3D) CFD solutions of the

geometrically correct feedback tanks and exhaust chambers as indicated in Figure 3.8. This results in an accurate simulation of the complex and time dependent pressure, temperature and velocity distributions inside the feedback tanks and exhaust chambers.

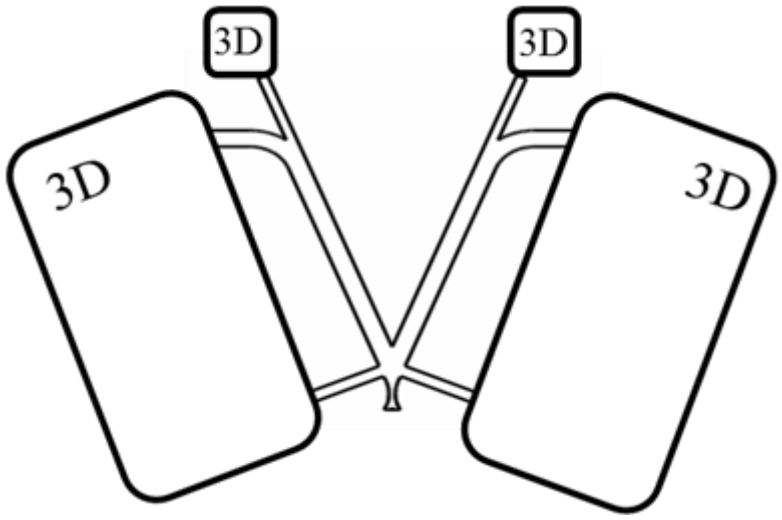

Figure 3.8: 2D/3D model of the supersonic fluidic oscillator

The design of the experimental SPF chamber used for comparison of the computational results requires the selection of pressure transducer and thermocouple locations. Therefore, the separate solutions for SPF chambers were initially conducted to yield design information regarding an experimental facility which has been constructed to validate this numerical method. It is not possible to completely incorporate the 3D Fluent solutions as UDFs as in the 0D/2D case. To overcome this issue, ANSYS Fluent is used in the server mode, which provides the ability to issue commands to more than one ANSYS Fluent session running at any one time. This allows the separate 2D and 3D ANSYS Fluent jobs to be run in such a way that they communicate with each other. One UDF in each model is used to feed the boundary conditions back and forth between Fluent jobs as shown in Figure 3.9. A connection is established between MATLAB and Fluent so that Fluent

commands are launched by the MATLAB session. The area weighted average velocity from the 2D oscillator model is fed into 3D model of the feedback tanks and SPF chambers and the solution is allowed to run for one time step. At the end of this time step, the volume averaged pressure change in the feedback tanks and SPF chambers is determined and returned back to the 2D CFD solution of the flow in the oscillator channels for the calculations for next time step. The turbulence parameters such as turbulence intensity and hydraulic diameter are held constant and are not transferred. All the data transfer between the Fluent jobs is done at the end of each time step and there are no iterations between the transfer of data from one model to the other. This arrangement allows the local changes inside the feedback tanks and the SPF chambers to be monitored. The transient solution is run with a 10^{-4} second time step. The MATLAB code for executing Fluent commands from MATLAB session is given in the Appendix B.2.

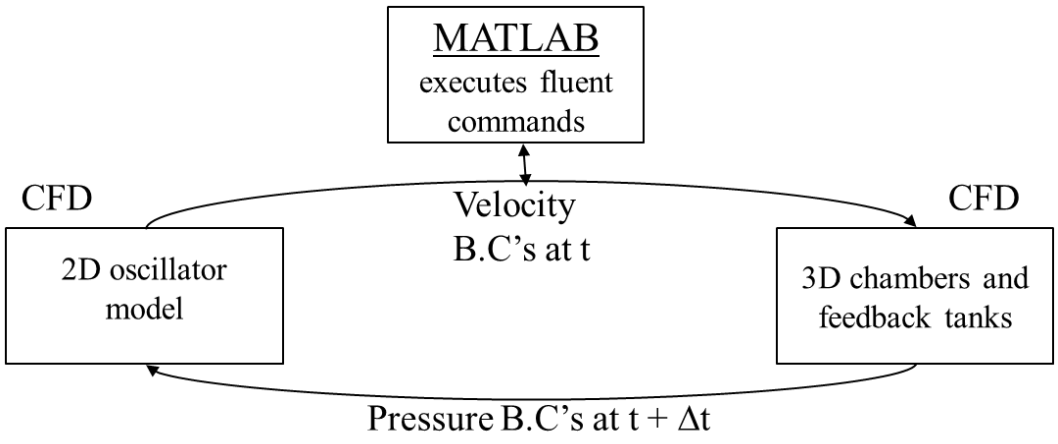

Figure 3.9: Control logic for MATLAB-ANSYS Fluent coupling

The 2D/0D CFD model mesh is used to determine the flow in oscillator channels and a 3D mesh is generated for the feedback tanks and the exhaust chambers. An unstructured mesh is generated over the entire domain of each tank and is further converted

into polyhedral cells to lower the overall cell count. The symmetry boundary about the inlet is also used to reduce the extent of computational model to a symmetric subsection of the full-scale feedback tank. A similar approach is used for the SPF chambers.

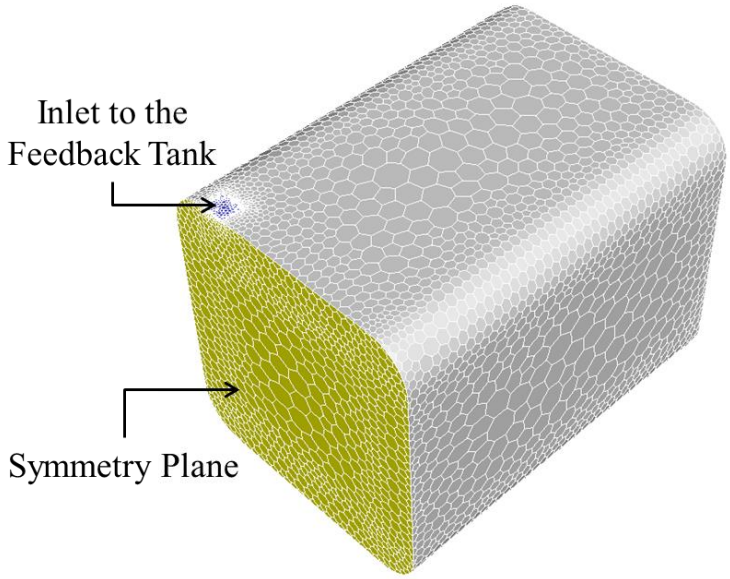

Figure 3.10: Polyhedral mesh used for the numerical simulations of the feedback tank

The mesh is tested for grid independence for the tank filling problem. After the mesh sensitivity study, the mesh for the exhaust chambers and feedback tanks contained 97855 computational cells and 16034 computational cells respectively. Another mesh containing 228062 cells for the exhaust chambers and 37381 cells for the feedback tanks is used to estimate the mesh sensitivity. The refined mesh gives a relative change in the volume average total pressure within 2% and hence the coarser meshes are used. This gives a total number of computational cells for the final hybrid 2D/3D model as 290317, which is the addition of two 3D grids for the exhaust chambers (97855 cells each), two 3D grids for the feedback tanks (16034 cells each) and one 2D grid for oscillator channels (62539 cells).

The simulation runs in the transient mode with a $1x10^{-4}$ second time step since a time step of $1x10^{-5}$ seconds is found to give a relative change in the volume average total pressure of only 1.42% for the exhaust chamber and 1.13% for the feedback tank. This arrangement is used in the following investigations. The numerical solution methods are kept the same as those used in the 2D/0D model in order to have consistency in the two models.

Chapter 4 Results and Discussions

The results obtained from the numerical simulations for the Bi-Stable Load-Switched Supersonic Fluidic Oscillator are presented in this chapter. Firstly, the performance parameters of the supersonic fluidic oscillator are defined. A comparison is then made between the results obtained by two different hybrid models. The computational load and accuracy of the two numerical models are also compared. Further, the influence of various operating conditions is investigated on the performance of the oscillator using the 2-D/0-D model. A comparison with the concurrent experimental study is made to evaluate this numerical model and determine areas requiring improvement.

4.1. Determination of oscillator performance

Performance of the supersonic fluidic oscillator is specified using the following parameters:

- Amplitude and frequency of the oscillation in the feedback tanks and SPF chambers during filling.
- Dimensionless chamber back pressure range required to produce stable oscillations.

Simulations are conducted for different supply pressures, different feedback tank volumes and supersonic fluidic oscillator scales to determine their effect on the performance of the device. The pressure variation within the oscillation cycle is also studied. Animations of the numerical flow field are generated and synchronized with pressure traces at various locations within the oscillator flow field using the numerical post processing software, DIAdem, to gain valuable insight into the oscillator operation. A parametric study of the fluidic oscillator is also conducted using dimensionless parameters:

dimensionless frequency and dimensionless pressure oscillation amplitude. The changes in these parameters are monitored with the increase in dimensionless SPF chamber pressure.

4.2. Non-dimensional parameters

In the post processing of the numerical results, normalization of some flow variables is implemented. The frequency and pressure amplitude are normalized in order to make more appropriate comparisons of the numerical and experimental results. This makes it easier to identify the trends on dimensionless plots of any variable.

4.2.1. Dimensionless frequency

The frequency of the oscillator is determined as the reciprocal of the time between consecutive pressure peaks obtained from the feedback tank pressure traces. The dimensionless frequency is defined in Equation 4.2.1,

$$F = {}^{fV_{fb}\rho}\Big/_{\dot{m}_s} \tag{4.2.1}$$

where, f is the frequency of oscillation, V_{fb} is the volume of the feedback tank, ρ is the density of the air in the supply reservoir and $\dot{m}_s$ is the supply mass flowrate.

4.2.2. Dimensionless pressure

Pressures anywhere in the solution are made dimensionless by dividing by the supply pressure. Hence, the dimensionless chamber back pressure is indicated in Equation 4.2.2,

$$\wp_b = {}^{P_b}\Big/_{P_s} \tag{4.2.2}$$

where, P_b and P_s are the chamber (back) pressure and supply pressure respectively.

4.2.3. Dimensionless pressure oscillation amplitude

The amplitude of pressure oscillation in either the feedback tank or exhaust chamber is defined as the peak-to-peak fluctuation of the pressure about the mean pressure as the pressure increases over one cycle.

$$\wp_{amp} = {(P_{max} - P_{min})_{cycle}}/{P_s} \tag{4.2.3}$$

Where, P_{max}, P_{min} and P_s are the maximum pressure in one cycle, minimum pressure in one cycle and supply pressure respectively.

4.3. Comparisons of numerical results of the two hybrid models

Numerical simulations are conducted under the same conditions of supply pressure and chamber back pressure. Of particular interest is whether the 2D/0D hybrid model provides frequency, feedback tank pressure amplitude and SPF chamber pressure amplitude results within an acceptable tolerance compared to those obtained from the 2D/3D hybrid model. The computational loads for the two models, as indicated by the required amount of computer memory and computational time, are also compared.

The supply pressure is held constant at 6.89 MPa (1000 Psi) gage and the initial chamber back pressure is set at 0.76 MPa (110 Psi) gage in both the cases. In 2D/0D model, the entire range of oscillation is captured while the calculation time involved in 2D/3D hybrid model is significantly higher than the 2D/0D model, and hence, only particular sections of the oscillation range are captured to give the overall trend.

The dimensionless frequencies predicted by the two numerical models for a supply pressure of 6.89 MPa (1000 Psi) gage are plotted against the dimensionless chamber pressure in Figure 4.1 for comparison.

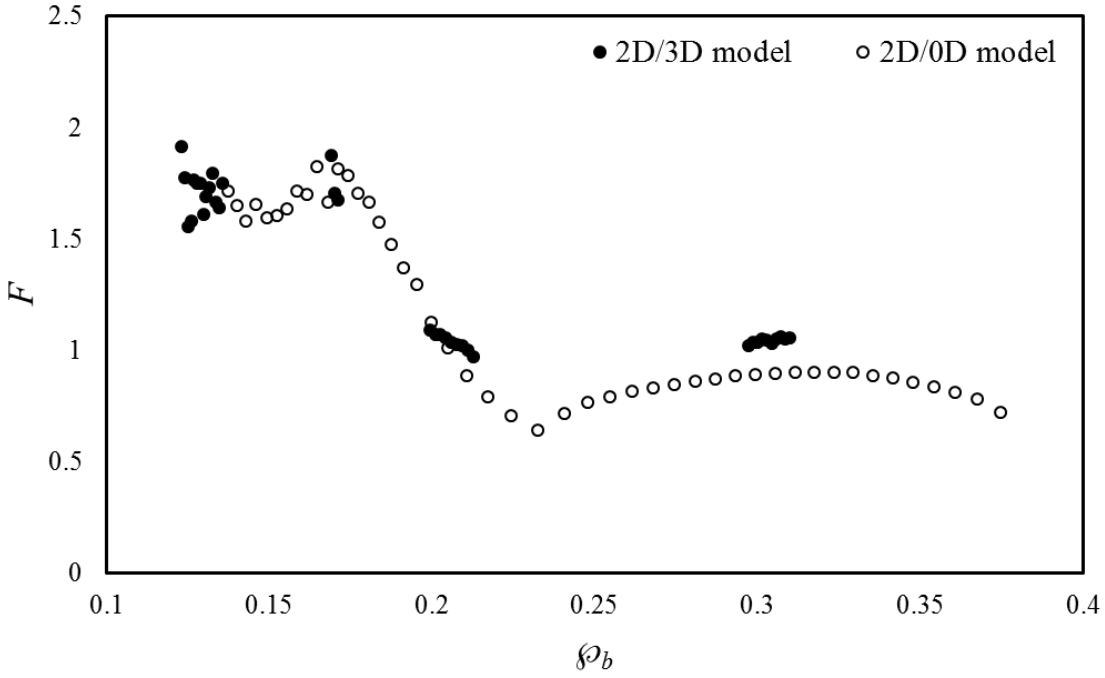

Figure 4.1: Dimensionless frequency versus dimensionless chamber pressure

It is seen that similar trends in dimensionless frequency are predicted with the two models. The 2D/3D model gives slightly higher values than those predicted by the 2D/0D model especially at higher values of chamber pressure. The difference may be due to the different assumptions regarding the transfer of heat to the surroundings from the feedback tanks and exhaust chambers that are made for the two cases. The 2D/0D model assumes a perfect isothermal process, which means that there is always enough heat transfer from the chamber or tank to maintain the same temperature everywhere inside. The 2D/3D model assumes an isothermal condition only for the walls, but not for the contained fluid. This

results in less energy loss to the surroundings in the 2D/3D model than 2D/0D model, which leads to a more rapid pressurization of the tanks and chambers in this case.

For small values of dimensionless chamber pressure (less than approximately 0.13) there are no oscillations and the jet divides equally into the two outlet channels. The resulting steady velocity contours are shown in Figure 4.2. In this region, the supply pressure is very large relative to the chamber pressure making the jet momentum the dominant controlling factor and the Coanda Effect is not strong enough to make the flow move to one of the two sidewalls and start the oscillation.

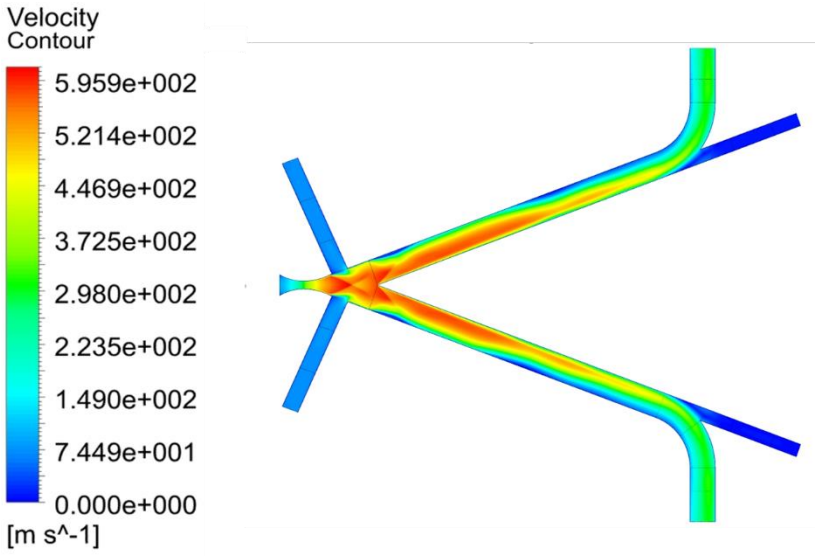

Figure 4.2: Velocity contour showing the jet splitting equally into two outlet channels when dimensionless chamber back pressure (0.125) is not large enough to start the oscillation.

As the dimensionless chamber pressure is increased, in the range of approximately $0.13 < \wp b < 0.175$, the division of the jet at the splitter becomes unstable and small oscillations begin. The velocity contours for a dimensionless chamber pressure of 0.15 at

the beginning of the cycle, ¼ of the cycle and ½ of the cycle are shown in Figures 4.3 (a), (b) and (c) respectively. The frequency of the oscillation in the given case is 48.54 Hz. This frequency is high because of the high momentum jet, which does not allow the jet to bend completely about the splitter tip.

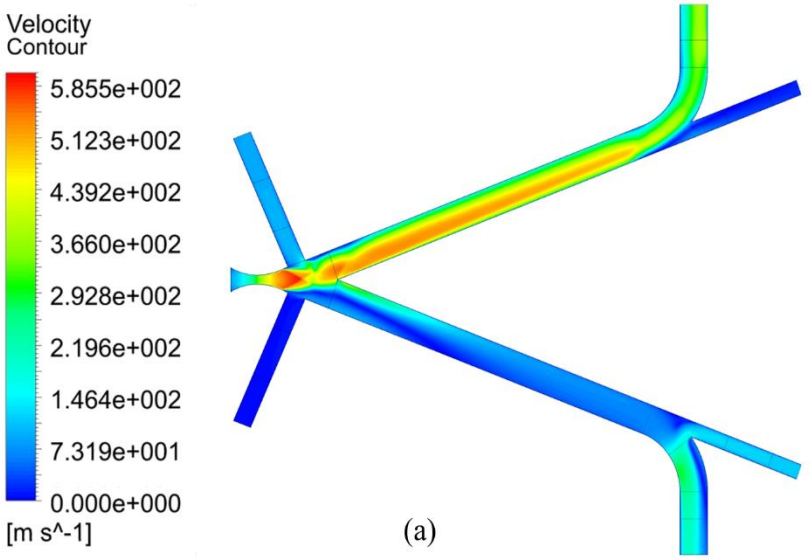

(a)

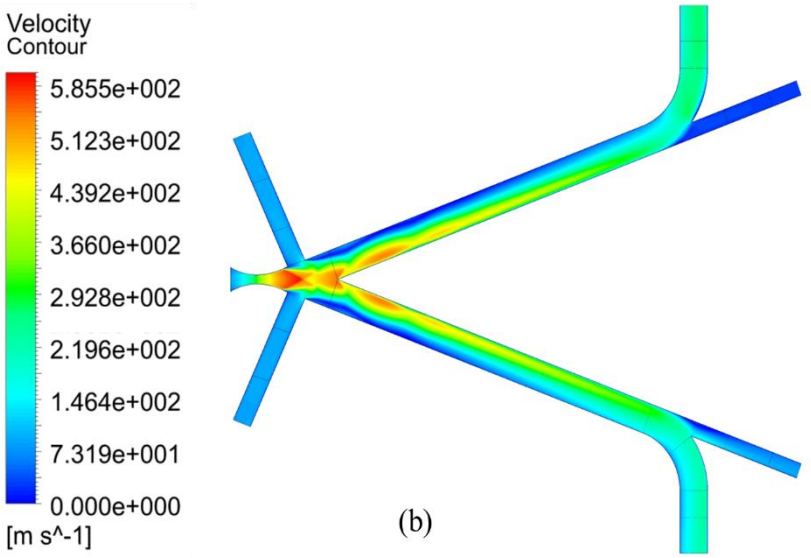

(b)

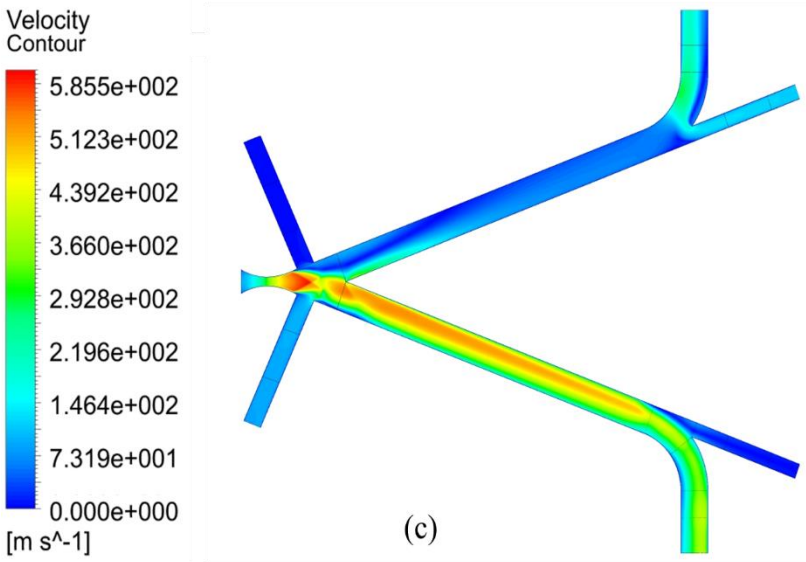

Figure 4.3: Velocity contour showing the jet oscillation when dimensionless chamber back pressure is 0.15 (a) beginning of the cycle, (b) ¼ of the cycle and (c) ½ of the cycle

A further increase of the dimensionless chamber pressure, in the range of approximately $0.175 < \wp b < 0.225$, reduces the jet momentum, increases the angular jet displacement which reduces the oscillation frequency and allows the Coanda Effect to begin to have an influence. In this region, the frequency and amplitude of the oscillation vary considerably.

Once the angular displacement amplitude is large enough, further increases in the dimensionless chamber pressure, in the range of approximately $0.225 < \wp b < 0.4$, cause the jet to attach to the side walls and the Coanda Effect does not significantly affect the cycle period. In this region, the frequency almost stays constant with an increase in dimensionless chamber pressure. The velocity contours for a dimensionless chamber pressure of 0.33 at the beginning of the cycle, ¼ of the cycle and ½ of the cycle are shown in Figures 4.4 (a), (b) and (c) respectively. The frequency of the oscillation in the given case is 25.57 Hz.

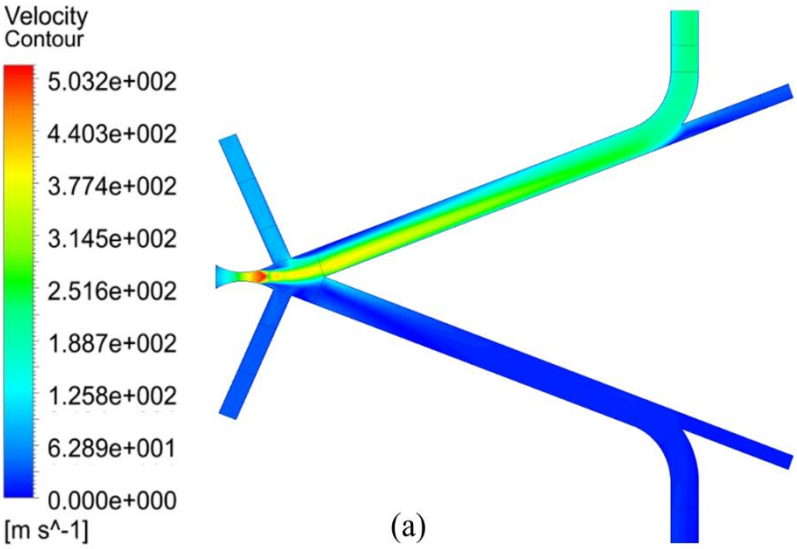
Velocity
Contour
5.032e+002
4.403e+002
3.774e+002
3.145e+002
2.516e+002
1.887e+002
1.258e+002
6.289e+001
0.000e+000
[m s^-1]

(a)

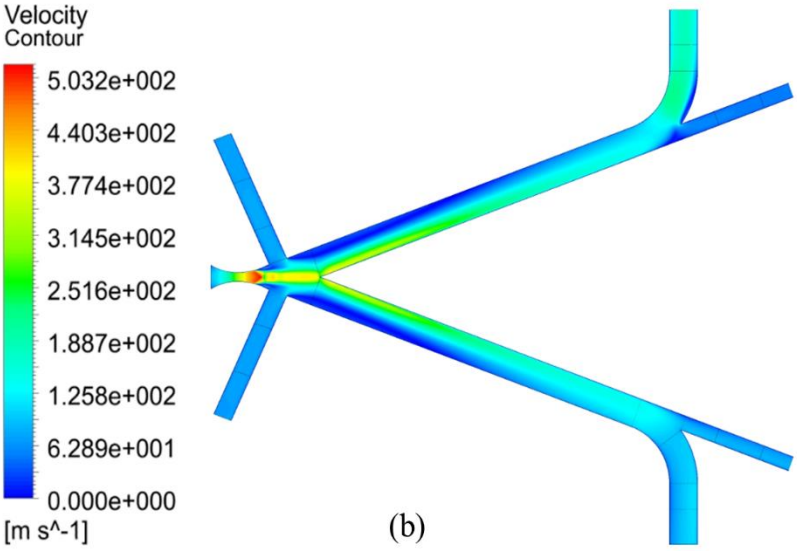
Velocity
Contour
5.032e+002
4.403e+002
3.774e+002
3.145e+002
2.516e+002
1.887e+002
1.258e+002
6.289e+001
0.000e+000
[m s^-1]

(b)

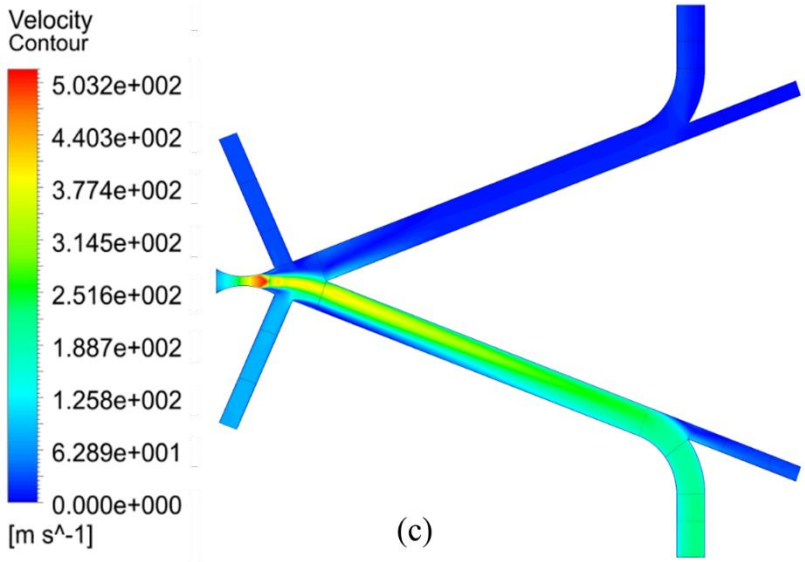

Figure 4.4: Velocity contour showing the jet oscillation when dimensionless chamber back pressure is 0.33 (a) beginning of the cycle, (b) ¼ of the cycle and (c) ½ of the cycle

At very high values of dimensionless chamber pressure (greater than approximately 0.4) the frequency reduces drastically (not shown in Figure 4.1). The flow remains attached to one side of the oscillator for longer period. Eventually, the oscillations stop as the uniform pressure is reached throughout the system. This region is not of interest in the current application.

For this supply pressure, a comparison of the pressure oscillation amplitudes in feedback tanks and chambers for the two numerical models are presented in Figures 4.5 and 4.6 respectively.

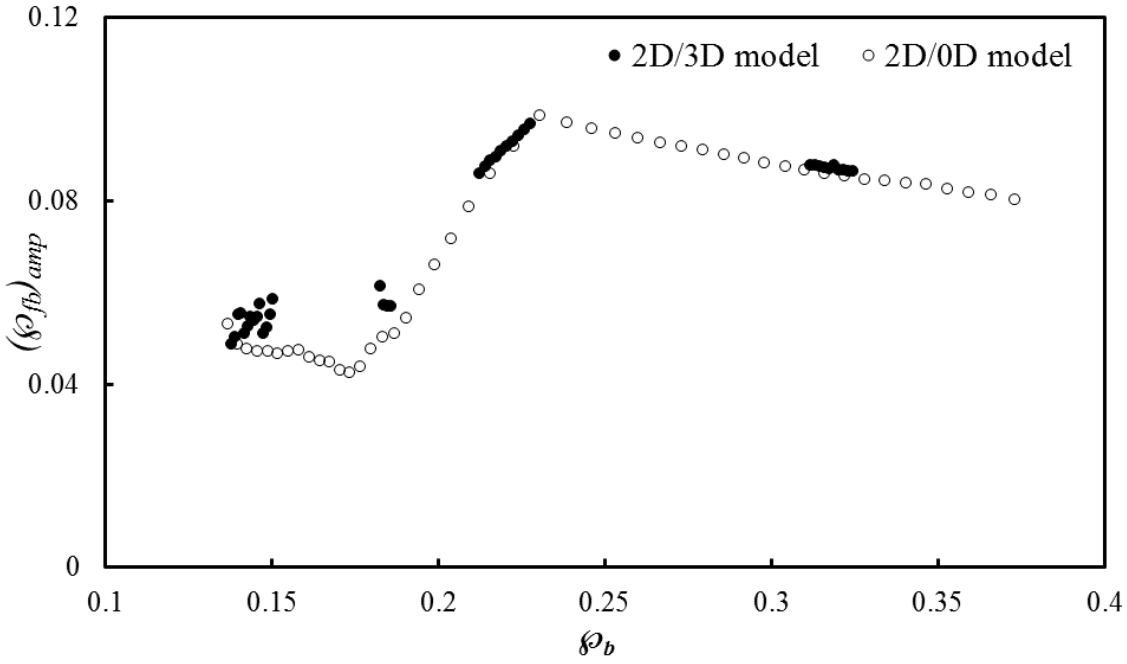

Figure 4.5: Dimensionless feedback tank pressure amplitude versus dimensionless chamber pressure

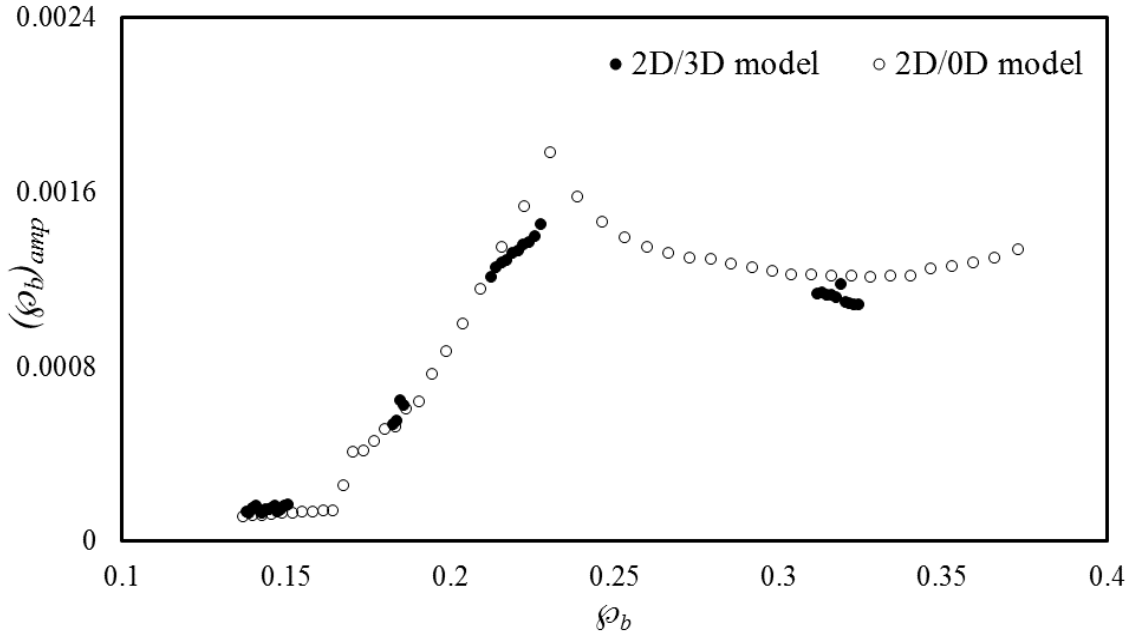

Figure 4.6: Dimensionless chamber pressure amplitude versus dimensionless chamber pressure

These diagrams exhibit the same three characteristic regions as the dimensionless frequency. In general, the amplitude of the oscillation increases with the decrease in frequency. Lowering the cycle frequency gives more time for the flow to pass through one of the channels and fill the feedback tank and SPF chamber on that side of the oscillator. The dimensionless chamber and feedback tank amplitudes are approximately constant in the lowest range as the jet exhibits small oscillations about the splitter. The dimensionless amplitudes increase as the angular jet displacement increases in the intermediate region. The dimensionless amplitudes remain approximately constant during the period dominated by the Coanda Effect. Small deviations from these trends are thought to be due to changes in the pressure waveform shapes and control channel flows. The maximum amplitude of the pressure oscillation occurs near the center of the range of dimensionless chamber pressure in which oscillation occurs. Both models predict the similar trends in amplitude variation and there is not much difference in the dimensionless amplitude values predicted by two models.

The additional computational load involved in using the 2D/3D model is also investigated. The computational load is indicated by amount of memory and computational time required for the two hybrid models. The present 2D/0D hybrid model reduces a computational load significantly compared to the 2D/3D hybrid model and can predict the characteristics of flow with reasonable accuracy. The required memory is approximately proportional to the grid size [26]. Using the size information presented earlier, the 2D/3D model requires approximately 4.64 times the memory of the 2D/0D case. Based on a measurement of the actual computational times for the two cases, the 2D/0D model computational time is approximately 1/5 of that for the simulation of the 2D/3D hybrid

domain. Clearly, the 2D/0D hybrid model uses less computational time and space. The 2D/3D case, however, gives us a deeper insight to the flow variation inside the feedback tanks and exhaust chambers. The animation of total pressure variation inside the feedback tanks and SPF chambers shows that during operation, the total pressure distribution is very uniform everywhere inside the feedback tanks and SPF chambers except the region near the mass flow rate inlet/exits.

Since, the 2D/0D hybrid model requires significantly less computational load compared to the 2D/3D hybrid model while predicting the performance characteristics with reasonable accuracy. It was decided to complete the remainder of the numerical investigations using the 2D/0D hybrid model.

4.4. Internal flow phenomena of the Bi-Stable Load-Switched Fluidic Oscillator during an oscillation cycle at dimensionless chamber pressure of 0.18

In this section, the internal flow phenomena of the oscillator are shown in the form of streamlines for half period of an oscillation cycle. It should be noted that the streamline pattern for the second half of the oscillation cycle is a mirror image of the first half cycle. The computational results presented here are related to the corresponding feedback tank pressure to establish the relation between the feedback tank pressure and switching of flow from one channel to the other.

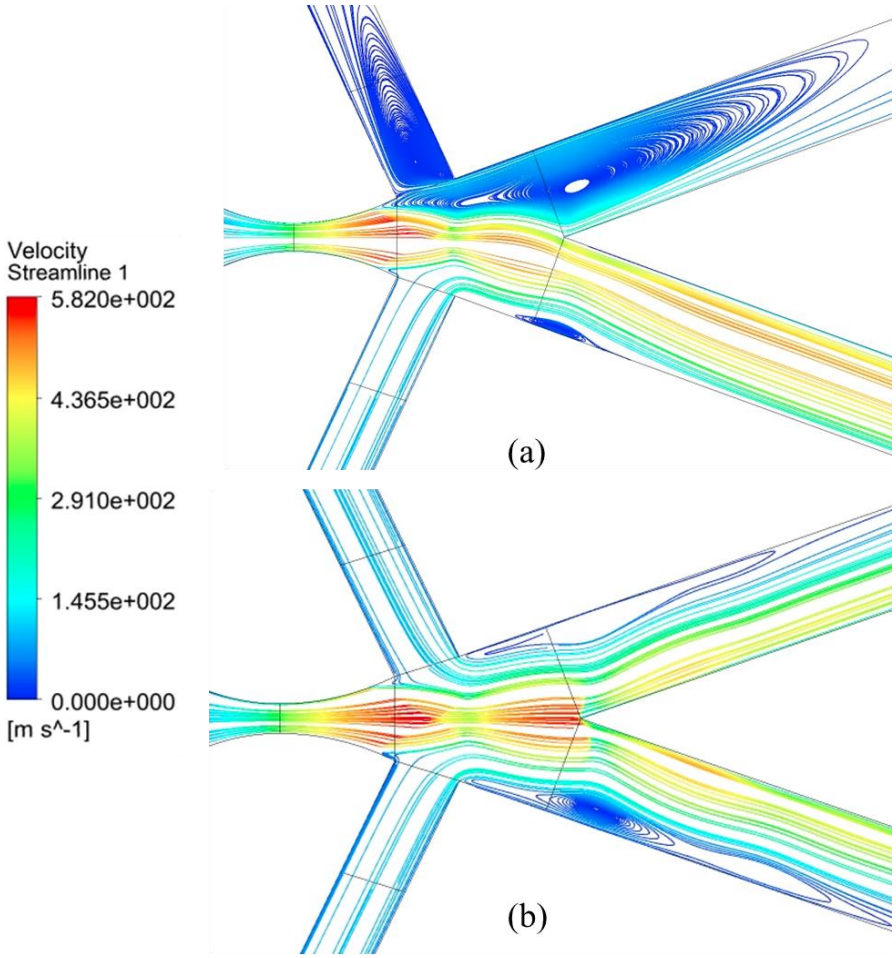
Velocity
Streamline 1
5.820e+002
4.365e+002
2.910e+002
1.455e+002
0.000e+000
[m s^-1]
(a)
(b)

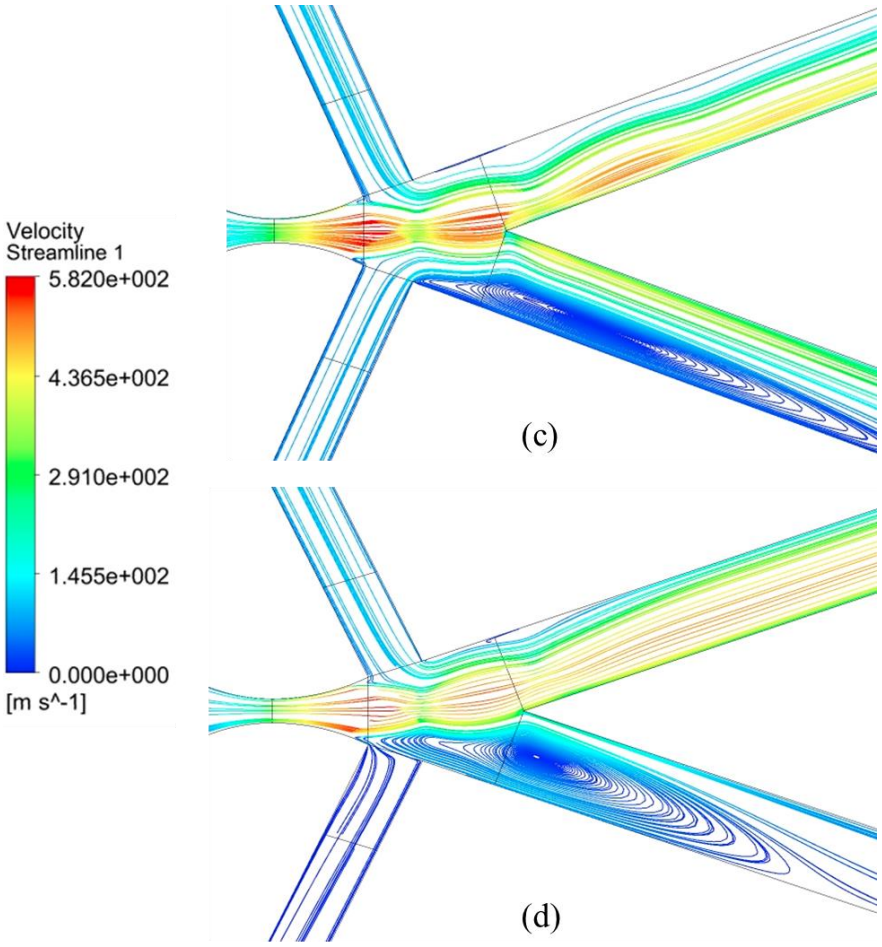

Figure 4.7: Numerical flow streamlines (a) when the flow is attached to the bottom channel, (b) when the flow is switching from one channel to the other, (c) recirculation region growing in the bottom channel, (d) when the flow is completely switched from lower channel to the upper channel

The numerical results shown in Figure 4.7 (a), (b) (c), and (d) are obtained using a 6.89 MPa (1000 Psi) gage supply pressure and SPF chamber pressure is set to 1.17 MPa (170 Psi) gage as the initial value. The dimensionless chamber pressure at this stage is 0.18 and this region is dominated by the Coanda effect. This combination of supply pressure and SPF chamber pressure can generate stable oscillation. The direction of the flow is from left to right in all the cases. Supply pressure is held at a constant value, while the SPF

chamber pressure is allowed to increase as the chambers start filling during the process. The flow enters from the inlet of the converging-diverging nozzle and attaches to the lower wall due to the Coanda Effect as shown in Figure 4.7 (a). As a result, the feedback tank on the attached side starts pressurizing while the one on the other side, is being de-pressurized. The pressurization of the lower feedback tank builds up the pressure downstream in the lower channel, such that it starts restricting the flow entering the lower feedback tank and begins to switch the flow to the other side of the oscillator. A recirculating region near the entrance of the lower channel becomes larger with time as the consequence of the switch as seen in Fig. 4.7 (b). This increase in recirculating region size reduces the curvature of the streamlines and pushes the reattachment point further downstream.

The region of flow recirculation continues to grow as shown in Fig. 4.7 (c) and finally blocks the lower channel as shown in Fig. 4.7 (d). The main flow has now completely switched to the other side of the oscillator. After the flow switches, the pressure in the upper channel increases. This pressure rise pushes the reattachment location closer to the inlet and reduces the recirculating region to a negligible size in upper channel. This process completes a half-cycle of the oscillation. After the switch, the built-up downstream pressure in the lower channel dissipates, and the same process occurs on the opposite side of the oscillator. Due to the symmetry of the device, the jet will oscillate between the two side walls in a periodic manner. Qualitatively, the flow fields predicted by the present analysis are in general agreement with the literature [4].

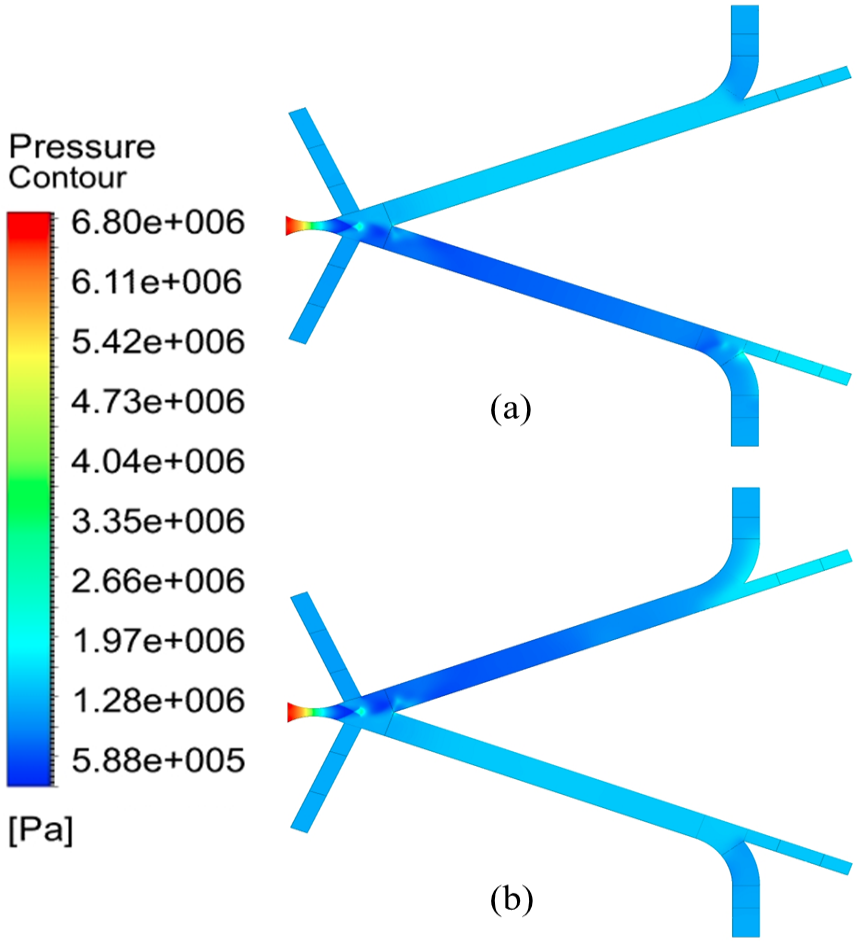

Figure 4.8: Static pressure contours (a) when the flow is attached to the bottom channel (b) when the flow is completely switched from lower channel to the upper channel

The flow structure discussed above in Figure 4.7 (a), (b) (c), and (d) is confirmed by the static pressure contours shown in the Figure 4.8 (a) and (b). The pressure contours in Figure 4.8 (a) and Figure (b) correspond to Figure 4.7 (a) and Figure 4.7 (d) respectively. The pressures in the lower channel are very low when the flow is passing through this channel (Fig. 4.8 (a)). Similarly, the pressures in the upper channel are very low when the flow is passing through this channel (Fig. 4.8 (b)).

4.5. Shock diamond analysis

The boundary conditions for this analysis are the same as those specified in the previous section. Time-dependent velocity contours and pressure distribution contours are shown to visualize the internal flow pattern of the supersonic fluidic oscillator to locate the shock diamonds. Figure 4.9 shows the velocity magnitude contour at one instance when the main flow jet is attached to the upper output channel. The shock diamond appears in the divergent section of the nozzle after the flow separation. The shock wave is seen to produce a finite deceleration of the flow to lower speed over a very small distance after the shock diamond. The following shocks are seen to be not as strong as the first one as their velocity gradients are not as large. There is an oblique shock seen at the flow splitter and thereafter, no shock waves are found inside the flow channels. None of the shock waves reach the feedback tanks or the SPF chambers. Similar patterns are seen in the static pressure contours shown in Figure 4.10.

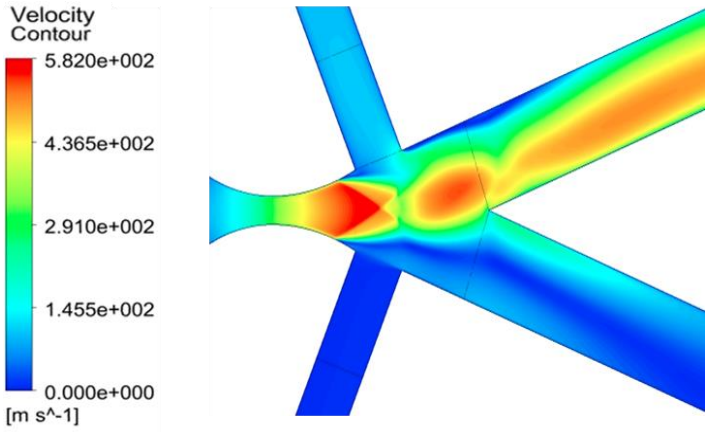

Figure 4.9: Instantaneous velocity magnitude contours of the internal flow field of the supersonic fluidic oscillator

The pressures in the upper output channel are slightly less than those in the lower output channel as shown in Figure 4.10. When the main flow jet separates from the divergent walls, supersonic exhaust from the converging-diverging nozzle is slightly over-expanded which means that the static pressure of the flow exiting the nozzle is less than the back pressure. The higher back pressure compresses the flow, this compression increases the pressure of the flow substantially. However, this compression of the flow increases the pressure too much so that it exceeds the back pressure. As a result, the flow now expands back outward to reduce the pressure again. Therefore, the subsequent series of expansions and compressions results in the formation of shock diamond patterns downstream. The numerical result gives a very similar flow pattern as seen in the Schlieren images in the literature; see Figure 4.1 on page 38 of reference [4].

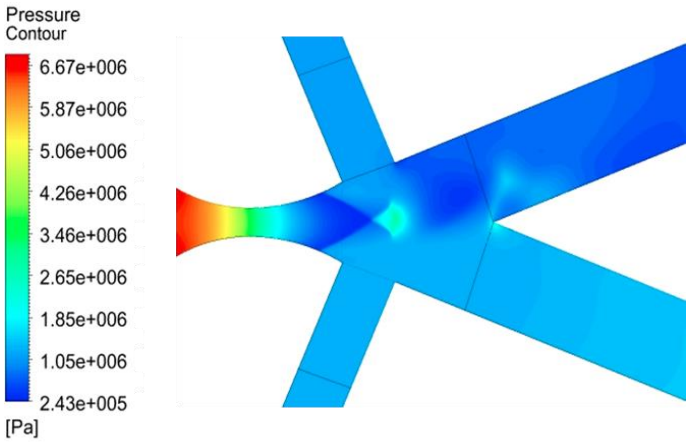

Figure 4.10: Instantaneous pressure distribution contours of the internal flow field of the supersonic fluidic oscillator

4.6. Influence of various operating parameters on oscillator performance

This section includes an investigation of the effect that a range of operating parameters, such as the working fluid, supply pressure to chamber back pressure ratio, feedback tank volume has on the oscillator performance.

4.6.1. Influence of the working fluid

Numerical simulations are carried out for different flow conditions, where air and nitrogen are used as working fluids. The oscillation frequencies are calculated and compared for both the cases. The density and viscosity are taken to be: 1.225 kg/m^3 and 1.78 x 10^{-5} kg/m s^{-1} respectively for air, and 1.138 kg/m^3 and 1.66 x 10^{-5} kg/m s^{-1} respectively for nitrogen. Results for a supply pressure of 0.41 MPa (60 Psi) gage and a chamber with an initially atmospheric back pressure are presented in Figure 4.11.

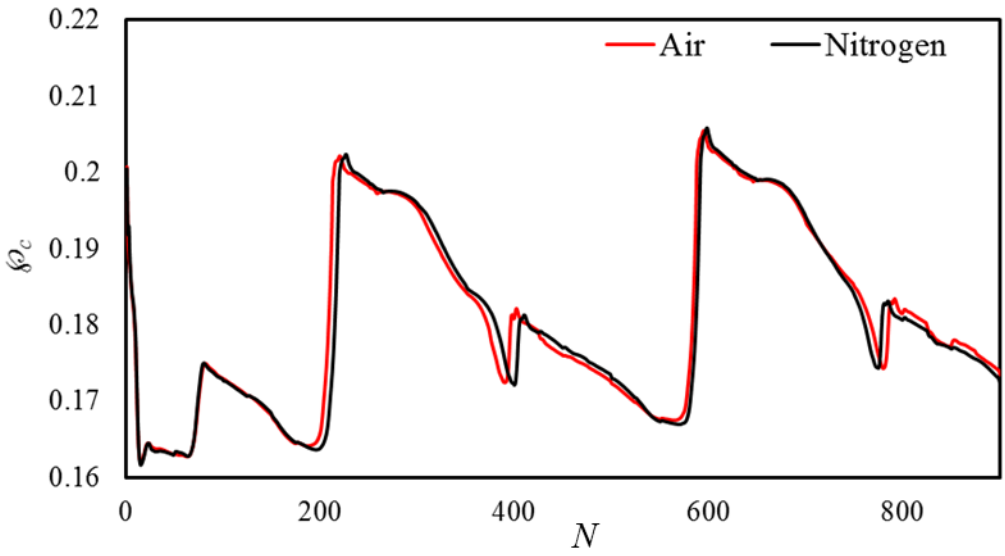

Figure 4.11: Dimensionless control port pressure versus number of time steps

It can be seen that for the given conditions there is very little difference in the frequencies calculated for air and nitrogen. The frequency calculated for air is 26.67 Hz

and 26.95 Hz for nitrogen. The percentage difference is approximately 1%. The jet oscillation frequencies are slightly higher when nitrogen is used as working fluid. The rate at which the pressure increases in the feedback tank is given by Equation 6 and is proportional to the gas constant which is larger for nitrogen. This makes the feedback tank on attached side to fill faster which makes the main jet stream to switch to the other attachment wall. Chamber pressure amplitudes and feedback tank pressure amplitudes calculated in both the cases are similar and are not shown here. Since, there is little difference in the results when air or nitrogen are used as flow medium, most of the simulations included in this thesis are performed using air as the working fluid.

4.6.2. Ideal gas versus real gas assumption

At very high-pressure or very low-temperature conditions the gases deviate from the ideal gas behavior. Therefore, flow cannot typically be modeled accurately using the ideal-gas assumption. The real gas model in Fluent allows you to accurately solve for fluid flow and heat transfer where the working fluid behavior deviates from the ideal-gas assumption. Ideal gas behavior can be expected when [25],

$$P/P_c << 1$$

or

$$T/T_c > 2 \text{ and } P/P_c < 1$$

Here, the subscript c stands for critical point where all the phases coexist in equilibrium. The critical point for nitrogen gas corresponds to T_c = 126 K and P_c = 3.4 MPa (492 Psi). In most places within the current oscillator, the temperatures and pressures in the ranges

which satisfy the ideal gas condition. The highest supply pressure tested is 6.89 MPa (1000 Psi). In this case, $^{P}/_{P_c}$ is greater than 1 and real gas effects will affect a portion of the field of flow. Figure 4.12 shows the numerical result for the supply pressure of 6.89 MPa (1000 Psi) gage and chamber back pressure is initially set at 1.172 MPa (170 Psi).

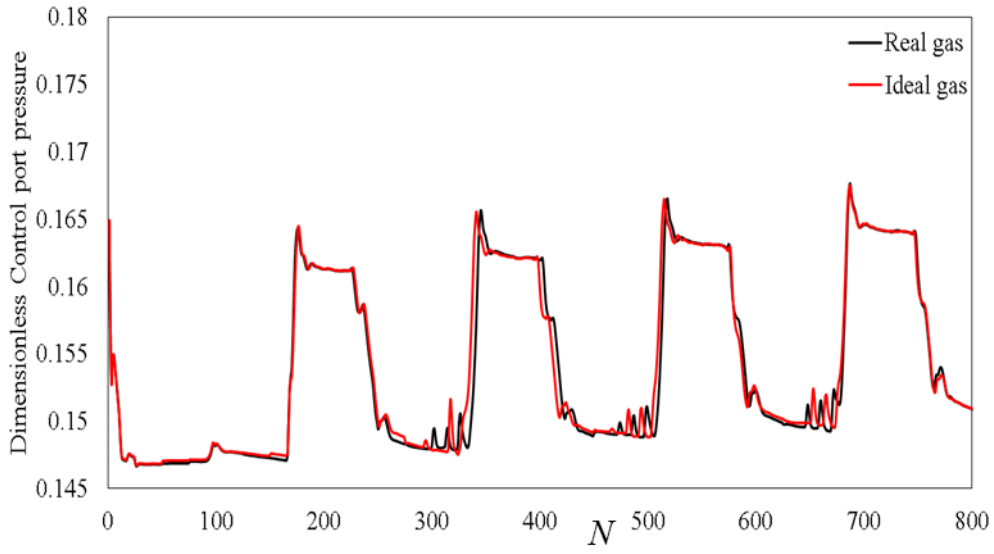

Figure 4.12: Dimensionless control port pressure versus number of time steps

For the given conditions there is not much difference in the control channel pressure calculated for both the ideal gas and real gas assumption. The flow is always choked at the throat of converging-diverging nozzle hence, the pressure at throat is approximately 0.528 times the supply pressure and decreases with the increase in flow velocity downstream as shown in Figure 4.13. Hence, a very small part of the flow field is affected by deviation of the gas behavior which is the reason there is not any noticeable difference in the results with both the assumptions. All the simulations included in this thesis are performed using ideal gas assumption.

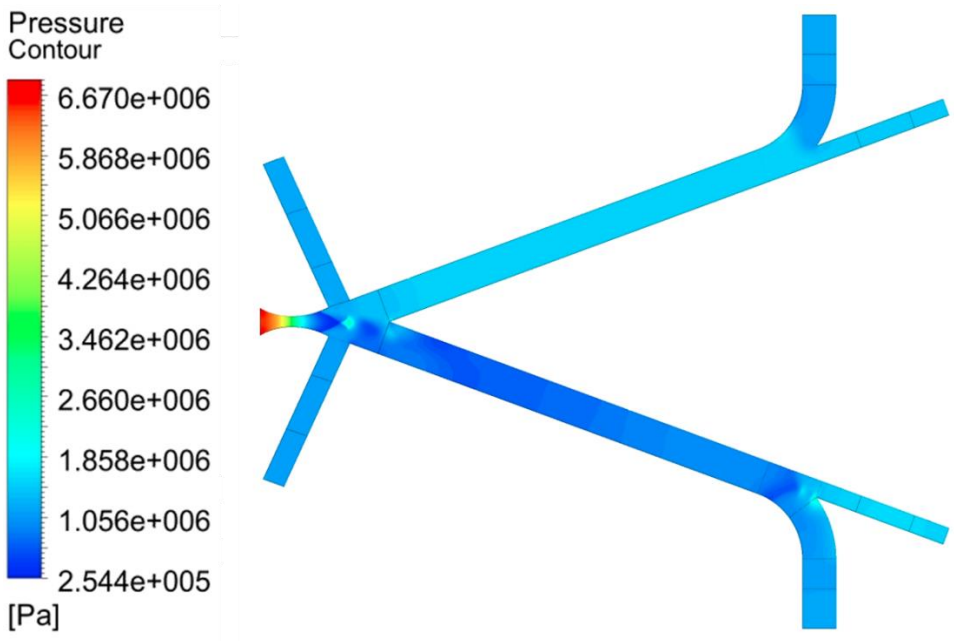

Figure 4.13: Instantaneous pressure distribution contour of the internal flow field when the flow is going through lower channel

4.6.3. Influence of the supply pressure to chamber back pressure ratio

The 2D/0D model is also used to determine the dimensionless chamber pressure range giving stable oscillation for air at three different values of the supply pressure. The simulations are performed holding the supply pressure at a constant value while the chambers fill, increasing the chamber back pressures. It was observed that the jet oscillation could only be produced in the certain range of the chamber back pressure. The dimensionless chamber pressure ratios at which stable oscillation starts and when it ends are presented in Table 1. It is important to note that the dimensionless chamber pressure is approximately the same for all supply pressures considered.

Supply Pressure P_s (Psi)	Minimum dimensionless chamber pressure for oscillations $(\wp_{b,})_{min}$	Maximum dimensionless chamber pressure for oscillations $(\wp_{b,})_{max}$
1014.7 (6.98 MPa)	0.140	0.400
544.7 (3.75 MPa)	0.138	0.398
112.7 (0.78 MPa)	0.135	0.378

Table 1: Effect of the dimensionless chamber back pressure on the range of oscillation

When the dimensionless chamber back pressure is less than approximately 0.14, the jet symmetrically splits into both output channels and no oscillation occurs. If the dimensionless chamber pressure is greater than approximately 0.4, the low momentum main jet flow attaches to one side and again, no oscillation occurs. Within the proper range of dimensionless chamber back pressure, the jet switches regularly between the two channels of the supersonic fluidic oscillator. These numerical results agree with the experimental observations of Xu; see Figure 4.20 on page 60 of reference [4] and McGeachy; see Figure 2 of reference [26] and Figure 8 of reference [28] . In their cases, back pressure is held constant at atmospheric pressure and supply pressure varied and jet oscillation only observed within the definite range of supply pressure.

4.6.4. Influence of the feedback tank volume

The effect of changing feedback tank volume size on the frequency of the oscillation is determined by holding the supply pressure constant at 0.68 MPa (98 Psi) gage supply pressure. The numerical results for 22 cc feedback tank volume and for 44 cc

feedback tank volume are shown in Table 2 and Table 3 respectively. It is noted that the oscillation frequency decreases and the chamber pressure oscillation amplitude increase with an increase of the feedback tank volume.

Chamber Pressure Ratio ($\wp_b$)	Chamber Amplitude (Psi)	Frequency (Hz)
0.13	0.012 (0.083 kPa)	58.14
0.175	0.015 (0.103 kPa)	54.05
0.22	0.055 (0.38 kPa)	31.45

Table 2: Oscillation performance at different chamber pressure ratios for feedback tank volume of 22 cc

Chamber Pressure Ratio ($\wp_b$)	Chamber Amplitude (Psi)	Frequency (Hz)
0.13	0.018 (0.124 kPa)	33.03
0.175	0.0298 (0.205 kPa)	28.82
0.22	0.114 (0.786 kPa)	15.02

Table 3: Oscillation performance at different chamber pressure ratios for feedback tank volume of 44 cc

The effect of changing feedback tank volume size on the frequency of the oscillation is also determined by holding the supply pressure constant at 0.41 MPa (60 Psi)

gage supply pressure with a constant atmospheric chamber back pressure. The numerical results are shown in Figure 4.14. The larger feedback tank volume delays the time needed for the deflected jet to move from one attachment wall to the opposite one, hence, reducing the frequency. The decrease in frequency is approximately linear with the feedback tank volume. The trend of decreasing frequency with increase in feedback tank volume has good agreement with Hiroki; see Figure 13 of the reference [23] and Xu: see Figure 4 of the reference [22].

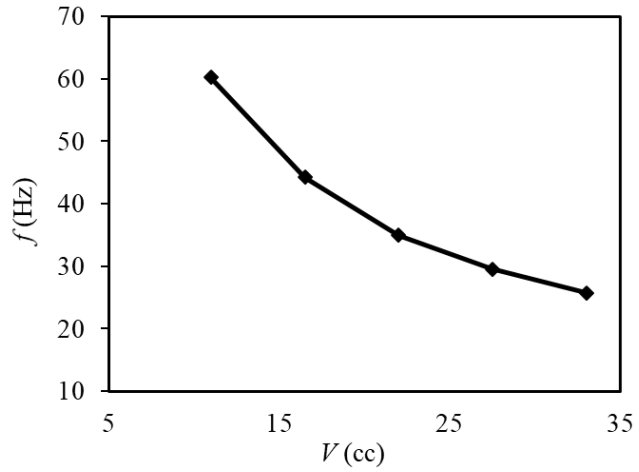

Figure 4.14: Oscillation frequency versus feedback tank volume

4.6.5. Influence of the polytropic index

The effect of different polytropic exponents on the tank filling processes in the SFO is studied by comparing the numerical simulation model results with those from the concurrent in-house experimental results [29]. The isothermal processes correspond to a polytropic exponent of n = 1 while for the isentropic processes it is n = 1.4. In the isentropic case there is no heat transfer from the tanks to the surroundings while in the isothermal case the heat transfer is just enough to maintain a constant temperature. The experimental curves are expected to be between the isothermal and isentropic curves. As shown in Figure

4.15, the chamber filling speed is close to the adiabatic assumption in the numerical solution. This means that the chamber filling process is approximately isentropic.

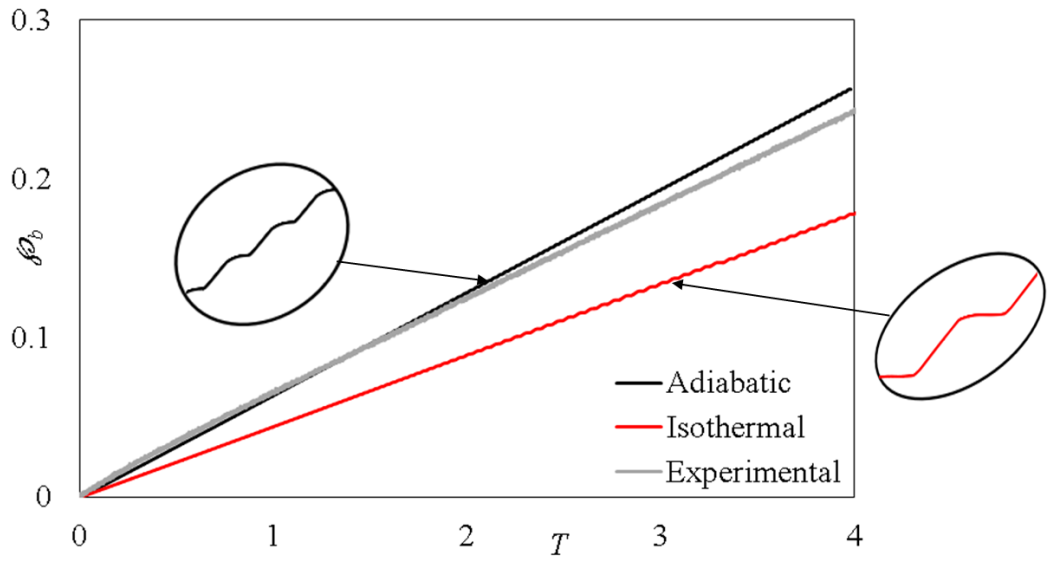

Figure 4.15: Dimensionless chamber pressure as the function of time

As evident from the figure, the adiabatic assumption of the flow gives higher frequency than the isothermal assumption. The pressure oscillation amplitudes are smaller in adiabatic case than in the isothermal case. Less energy losses in the adiabatic chamber filling process leads to the faster pressurization of the chambers with higher frequency and lower pressure oscillation amplitudes.

4.7. Effect of geometry scaling on oscillator performance

This section focuses on understanding the effects of geometry scaling on supersonic fluidic oscillator performance, with a particular emphasis on the frequency of the oscillator under various geometric and supply pressure conditions. Scaling studies are performed in order to establish the dimensionless criterion of the scaling data that will help provide further insight into the driving mechanism of the oscillations. This information is also

important in the design of supersonic fluidic oscillators for different applications. The original model used in this study is referred to as the 1.0-scale model. The oscillator profile is scaled down by the factor of 0.75 which gives a throat area ratio of $A_{(0.75)}/A_{(1.0)} = 0.75^2$. The volume of the feedback tanks however, is changed such that $V_{fb(0.75)}/V_{fb(1.0)} = 0.75$ instead of the 0.75^3 required for complete geometrical scaling. This new model obtained is referred to as the 0.75-scale model.

Figure 4.16 shows the effect of the scaling factor on the frequency characteristics of the oscillator in the range of chamber back pressures studied. The choked flow rate at 6.89 MPa (1000 Psi) gage is approximately 0.0512 kg/s (kilograms per second) for the1.0-scale while it is 0.034 kg/s at 8 MPa (1160 Psi) for the 0.75-scale oscillator. The SPF chamber volume is held constant at 0.008 m^3 (8 liters) for a direct comparison. Since, the SPF chamber volume is much larger than the oscillator size, it does not affect the frequency of the oscillation. Decreasing the scale of the oscillator decreases the throat area and feedback tank volume. The supplied (choked) mass flow rate is proportional to the throat area and the supply pressure. Considering the definition of the dimensionless frequency, given in Equation 4.2.1, the following relationship is expected; $F_{1.0\text{-}scale} = 0.75*F_{(1.0\text{-}scale)corrected}$. If the dimensionless frequency is corrected in Figure 4.16, the two curves will approximately fall on top of one another. From the numerical results, as expected, the dimensionless frequency increases by approximately 25% when the scale is decreased by a factor of 0.75.

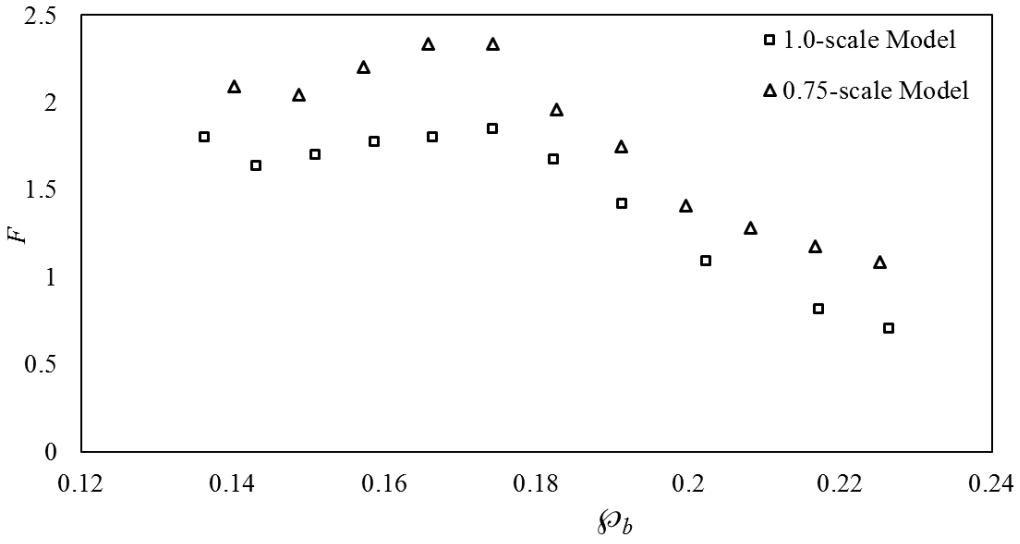

Figure 4.16: Dimensionless frequency versus dimensionless back pressure for different scale models

4.8. Frequency of the oscillation as the function of back pressure ratio

In this case the performance parameters of the supersonic fluidic oscillator are predicted for various values of supply pressure as the SPF chamber pressure is allowed to increase during the process. In the range of stable oscillation, the frequency is determined as the reciprocal of the time between consecutive pressure peaks obtained from the feedback tank pressure traces. All the frequency data for three different supply pressures within the range of oscillation is plotted against the dimensionless chamber back pressure in Figure 4.17. The supply pressures selected for comparison are 0.68 MPa (98 Psi) gage, 3.65 MPa (530 Psi) gage, and 6.895 MPa (1000 Psi) gage.

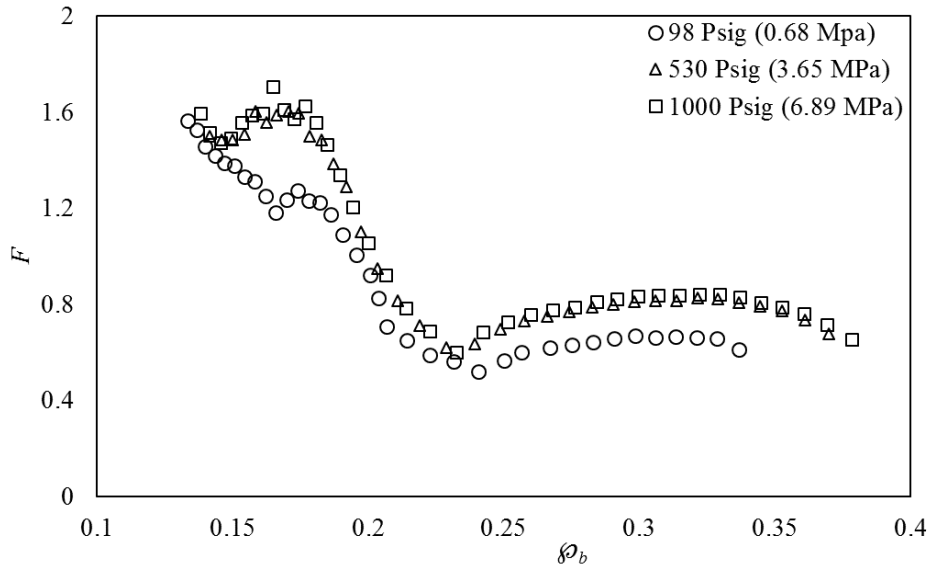

Figure 4.17: Dimensionless frequency response as the function of dimensionless chamber pressure

Similar trends in dimensionless frequency are seen for different supply pressures. As the supply pressure is increased to large values the dimensionless frequencies become nearly independent of supply pressure.

4.9. Amplitude of the oscillation as the function of back pressure ratio

In the range of stable oscillation, the amplitude of oscillation in either the feedback tank or SPF chamber is also determined by measuring the peak-to-peak fluctuation of the pressure about the mean pressure as the pressure increases over one cycle and is extracted from the CFD results. The supply pressures used in this comparison are the same as those specified in the previous section. All the pressure oscillation amplitude data in feedback tanks and SPF chambers for three different supply pressures within the range of oscillation are plotted against the dimensionless chamber back pressure in Figure 4.18 and Figure 4.19 respectively.

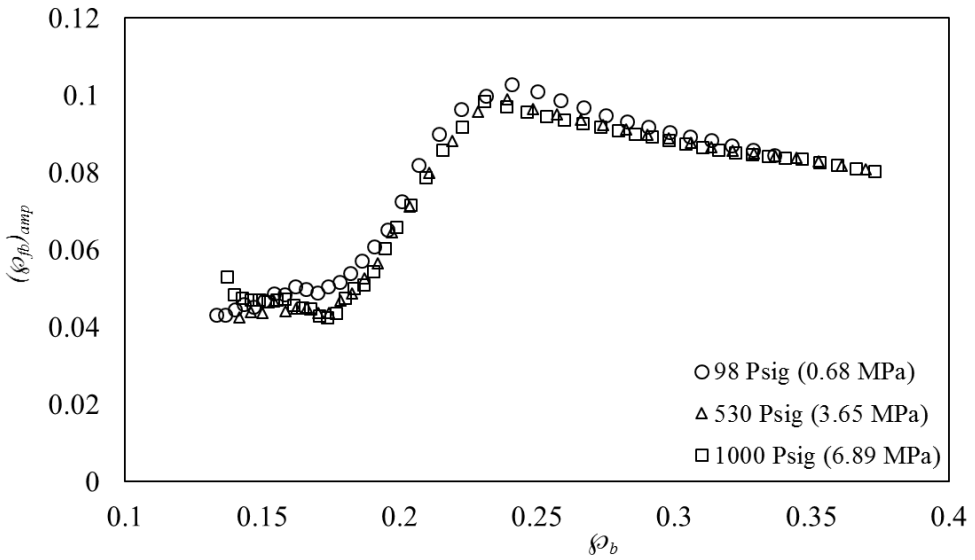

Figure 4.18: Dimensionless feedback tank pressure amplitude as the function of dimensionless chamber pressure

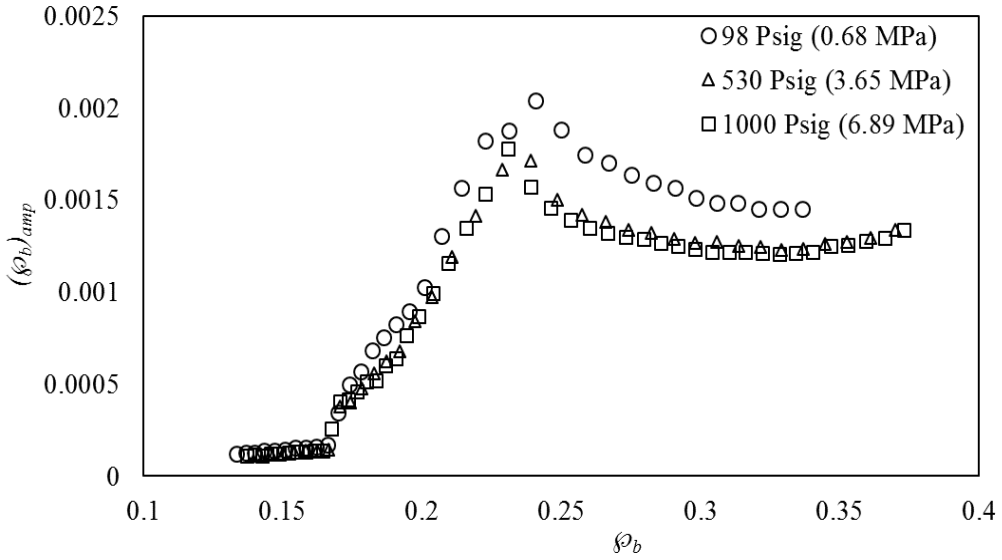

Figure 4.19: Dimensionless chamber pressure amplitude as the function of dimensionless chamber pressure

Similar trends in dimensionless feedback tank and chamber pressure amplitudes are seen for different supply pressures. In all the cases considered, the amplitudes are

approximately constant in the lower range. This region is governed by the momentum of the jet flow and the jet exhibits small oscillations about the flow splitter. Further increase in chamber back pressure reduces the jet momentum and the Coanda effect begins have an influence. This increase as the angular jet displacement and the flow spends more time on each side of the oscillator, giving more time for the flow on attached side to increase the feedback tank and chamber pressure. Once the angular displacement amplitude is large enough, further increases in the dimensionless chamber pressure do not affect the flow behavior significantly and dimensionless pressure amplitudes remain approximately constant in this region. Small deviations from these trends are thought to be due to changes in the pressure waveform shapes and control channel flows. Once the chamber pressure is high enough, the flow through control channels also begin to affect the driving mechanism of the oscillation. As shown in Figures 4.18 and 4.19, the maximum amplitude of the pressure oscillation occurs near the center of the range of dimensionless chamber pressure in which oscillation occurs.

4.10. Experimental validation

To validate the numerical results obtained in this study, the unsteady computational results are compared to available limited experimental data [29]. The chamber pressure data from the CFD solution is plotted along with the experimental results to compare the filling time in Figure 4.20. The supply pressure selected for comparison is 0.68 MPa (98 Psi) gage. The choked mass flow rate in the given case is 0.006 kg/s. It can be seen that the experimental and numerical result fall on top of each other and the maximum relative pressure difference at any given time is only 7.41 %.

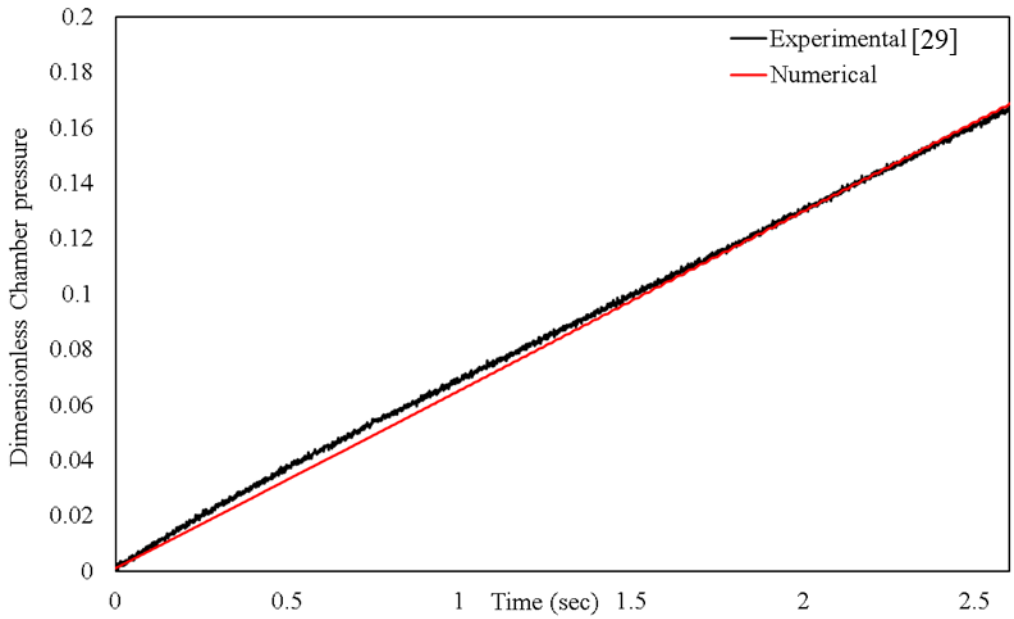

Figure 4.20: Dimensionless chamber pressure as the function of time

4.10.1. Comparison of the performance of the oscillator

For different back pressure to supply pressure ratios, the oscillation frequency varies in a range of 60 to 75 Hz compared to the numerical results which are in the range of 30 to 57 Hz. For the same back pressure to supply pressure ratio, the experimental results give a larger frequency. In Figure 4.21, the numerical results for dimensionless frequency are compared with experimental results for the supply pressure of 1.4 MPa (203 Psig) within the range of oscillation. Detailed discussion of the contents of Figures 4.21 - 4.23 has already been covered in Section 4.8 and 4.9. Here, the focus is to compare the numerical results with experimental results.

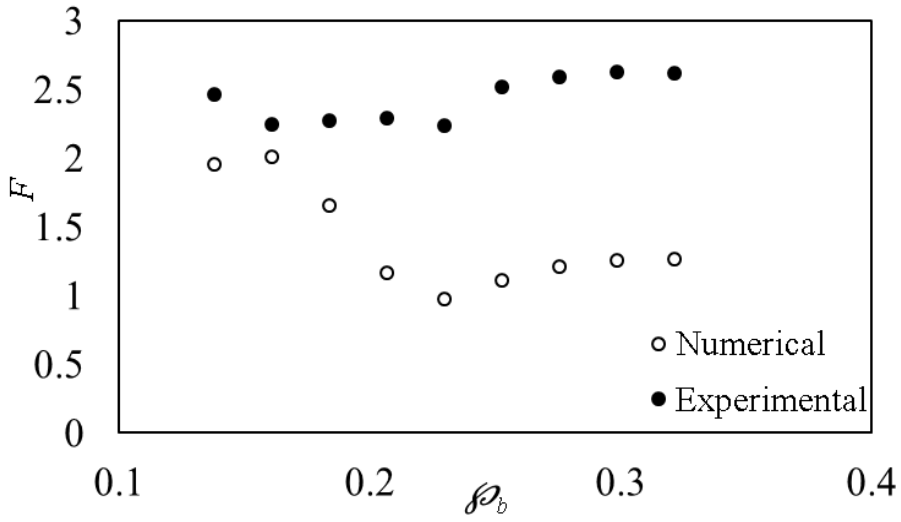

Figure 4.21: Dimensionless frequency as the function of dimensionless chamber pressure

In Figure 4.22, the numerical results for dimensionless chamber pressure amplitude is plotted against the dimensionless chamber back pressure for the supply pressure of 1.4 MPa (203 Psig) within the range of oscillation.

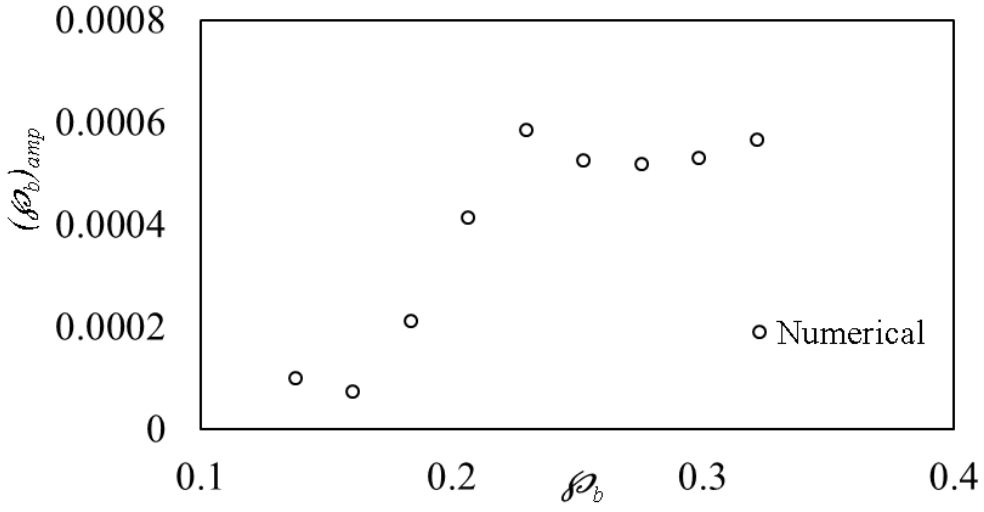

Figure 4.22: Numerical dimensionless chamber pressure amplitude as the function of dimensionless chamber pressure

Figure 4.23 shows the experimental results for dimensionless chamber pressure amplitude for the supply pressure of 1.4 MPa (203 Psig) and 1.03 MPa (150 Psig) within the range of oscillation.

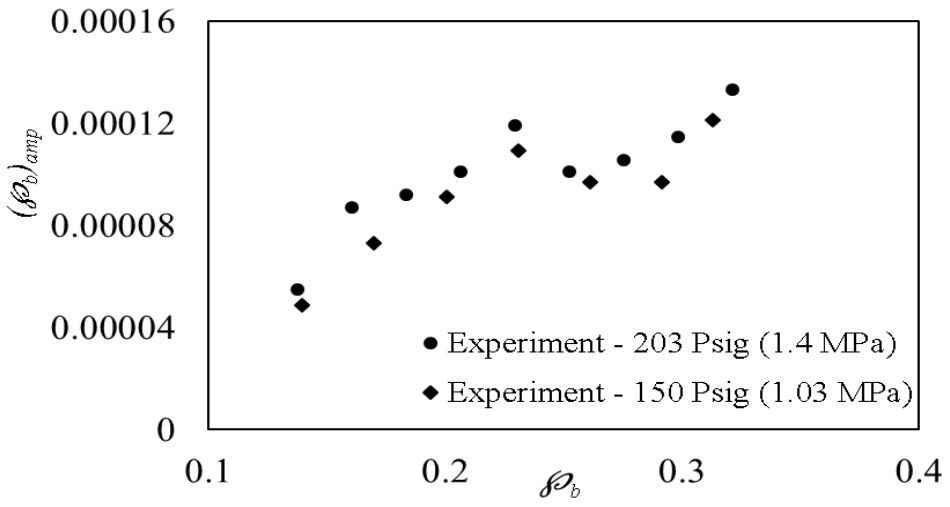

Figure 4.23: Experimental dimensionless chamber pressure amplitude as the function of dimensionless chamber pressure [29]

The experiment and the numerical model results have a similar trend, although the frequency is higher and amplitude in the experiments is much smaller than the numerical results. The numerical model, however, successfully captures the oscillation range ($0.13 < \wp_b < 0.4$).

In an effort to determine if the amplitude and frequency differences are due to an incorrect assumption of the loss coefficients in the 0D tank models, the model is run for a supply pressure of 1.4 MPa (203 Psi) gage and chamber back pressures of 0.14 MPa (20.3 Psi) gage and 0.21 MPa (30.3 Psi) gage with modified loss coefficients for the feedback and chamber channel filling and emptying. The results are given in Table 4.

Chamber Back Pressure (Psig)	Entrance Loss Coefficient	Exit Loss Coefficient	Frequency (Hz)	Amplitude (Psi)
20.3	0.5	0.5	58.14	0.016 (0.103 kPa)
20.3	0	0.5	65.79	0.022 (0.145 kPa)
30.3	0.5	0.5	33.22	0.09 (0.62 kPa)
30.3	0	0.5	38.76	0.075 (0.52 kPa)

Table 4: Effect of entry and exit losses on the oscillation performance at different chamber pressures

The experimental frequency and pressure oscillation amplitude is 67 Hz and 0.019 Psi (0.13 kPa) for 20.3 Psig chamber back pressure and 65 Hz and 0.024 Psi (0.16 kPa) for 30.3 Psig chamber back pressure respectively. It is seen that changing the loss coefficients effect the numerical solution considerably. The numerical results closely resemble the experiment at 20.3 Psig but not at 30.3 Psig. Therefore, constant values of loss coefficient do not adequately account for the losses. Correct incorporation of transient charge and discharge losses into the numerical model might help to bring the experimental and numerical results closer.

Chapter 5 Conclusions and Recommendations for Future Work

5.1. Conclusions

A numerical investigation of the performance characteristics of a Bi-Stable Load-Switched Supersonic Fluidic Oscillator is conducted using two hybrid models. The effects on the overall oscillation performance, which includes the oscillation frequency and the peak to peak feedback tank and SPF chamber pressure differences, are investigated using dimensionless parameters. The analysis gives the following conclusions:

1. Predicted frequencies and amplitudes of the oscillation follow similar trends in both the hybrid models and have values within 10 %.
2. The 2D/0D hybrid model requires significantly less computational load compared to the 2D/3D hybrid model while predicting the performance characteristics with reasonable accuracy. On the other hand, the 2D/3D model gives us deeper insight into the flow variation inside the feedback tanks and exhaust chambers.
3. The internal flow phenomena which occur in the Bi-Stable Load-Switched Supersonic Fluidic Oscillator during an oscillation cycle in the desirable oscillation region is investigated. The numerical model gives a reasonable prediction of the pressure gradient and location of the shock in the flow pattern. A shock is seen around the tip of the splitter and does not travel along the oscillator channels.
4. The range of dimensionless chamber pressure for which stable oscillations occur over a wide range of supply pressures is accurately predicted using the numerical models. For the given prototype of the Supersonic Fluidic Oscillator considered, this range is $0.13 < Pb/Ps < 0.40$.

5. For the given dimensionless chamber pressure, different characteristic regions are exhibited by the oscillator, as follows;
    a) $\wp b < 0.13$, there are no oscillations and the jet divides equally into the two outlet channels.
    b) $0.13 < \wp b < 0.175$, the division of the jet at the splitter becomes unstable and small oscillations begin.
    c) $0.175 < \wp b < 0.225$, the Coanda Effect begins to have an influence which increases jet displacement and lowers frequency.
    d) $0.225 < \wp b < 0.4$, the jet attach to the side walls for longer period. In this region, the frequency almost stays constant with an increase in dimensionless chamber pressure.
    e) $\wp b > 0.4$, frequency reduces drastically and eventually the oscillation stops.

    In general, the amplitude of the oscillation increases with the decrease in frequency.

6. The effects of changing working fluid, feedback tank volume, polytropic index and channel resistances on the performance of SFO indicated the following;
    a. Changing the working fluid from air to nitrogen didn't have any significant effect on the oscillator performance.
    b. Increasing the feedback tank volume decreases the frequency of the oscillation.
    c. Isentropic filling of the chambers is faster compared to the isothermal filling.
    d. Increasing the feedback and chamber back pressure resistances increased the frequency and lowered the amplitude of the oscillations.

7. The numerical model is capable of accurately predicting the frequencies when the oscillator scale is changed.
8. Similar trends in dimensionless frequency and amplitude are seen for different supply pressures. As the supply pressure is increased to large values, the dimensionless frequencies become independent of supply pressure.
9. The numerical and experimental results agree in trend for frequency and amplitude of the oscillation but consistently give lower frequency and higher amplitude of the oscillation. The numerical and experimental range of oscillation are approximately the same.

5.2. Recommendations for future work

Different scales of the oscillator should be validated in order to generalize the design parameters of the oscillator. The feedback tank and SPF chamber exit losses could be modified to account for the transient nature of the flow rather than specifying a constant value which is only accurate for high Re. A better method of accounting for the top and bottom wall frictional losses could be developed. The numerical model can be better validated for wide range of operating conditions of supply pressure. This simplified numerical model can be used to quickly give a reliable prediction of the oscillator performance within the acceptable error after validation for wide range of the experimental data.

References

[1] Black, J. T., and Kohser, R. A., *DeGarmo's Materials and Processes in Manufacturing*, 12th Edition, John Wiley & Sons, 2017.

[2] Cullen, G. W., and Korkolis, Y. P., "Ductility of 304 Stainless Steel under Pulsed Uniaxial Loading," International Journal of Solids and Structures, 50(10), 2013, pp. 1621–1633.

[3] Gokoglu, S., Kuczmarski, M., Culley, D., and Raghu, S., "Numerical Studies of a Supersonic Fluidic Diverter Actuator for Flow Control," Presented at the 5th Flow Control Conference 2010, Chicago, Illinois, USA, 2010.

[4] Xu, S., "Experimental Investigation of a Bi-Stable Supersonic Fluidic Oscillator," M.A.Sc. Thesis, Mechanical Engineering. University of Windsor (Canada), Windsor, Ontario, 2018.

[5] Gaylord, W., and Carter, V., *FLUERICS. 27. Flueric Temperature-sensing Oscillator Design,* HDL-TR-1428, Harry Diamond Labs, Washington D.C., 1969.

[6] Cerretelli, C., and Kirtley, K., "Boundary Layer Separation Control with Fluidic Oscillators," Journal of Turbomachinery, Vol. 131, No. 4, 2009, pp. 041001-041001–9. https://doi.org/10.1115/1.3066242.

[7] Ringwall, C. G., and Kelley, L. R., "Fluidic Temperature Sensor System", US Patent 3566689AMar 02, 1971.

[8] Shigang, L., Dailiang, X., and Shan, T., "Design and Simulation of Fluidic Flowmeter for the Measurement of Liquid Flow in Microchannel," Presented at the 2012 Third International Conference on Digital Manufacturing and Automation, Guilin, China., 2012.

[9] Bobusch, B. C., Berndt, P., Paschereit, C. O., and Klein, R., "Investigation of Fluidic Devices for Mixing Enhancement for the Shockless Explosion Combustion Process," In *Active Flow and Combustion Control 2014*, R. King, ed., Springer International Publishing, Cham, Switzerland, pp. 281–297, 2015.

[10] Raghu, S., "Fluidic Oscillators for Flow Control," Experiments in Fluids, Vol. 54, No. 2, 2013, https://doi.org/10.1007/s00348-012-1455-5.

[11] Raghu, S., "Feedback-Free Fluidic Oscillator and Method", US Patent US6253782B1, 2001.

[12] Campagnuolo, C. J., and Lee, H. C., *"Review of Some Fluid oscillators"*, Publication TR-1438. Harry Diamond Laboratories, Washington, D.C, 1969, p. 56.

[13] Panitz, T., and Wasan, D. T., "Flow Attachment to Solid Surfaces: The Coanda Effect," American Institute of Chemical Engineers Journal, Vol. 18, No. 1, 1972, pp. 51–57. https://doi.org/10.1002/aic.690180111

[14] Tesař, V., Peszynski, K., and Smyk, E., "Fluidic Low-Frequency Oscillator Consisting of Load-Switched Diverter and a Pair of Vortex Chambers," Presented at EPJ Web of Conferences., Prague, Czech Republic, Vol. 114, 2016, p. 02121.

[15] Simões, E. W., Furlan, R., Bruzetti Leminski, R. E., Gongora-Rubio, M. R., Pereira, M. T., Morimoto, N. I., and Santiago Avilés, J. J., "Microfluidic Oscillator for Gas Flow Control and Measurement," Flow Measurement and Instrumentation, 16(1), 2005, pp. 7–12. DOI: https://doi.org/10.1016/j.flowmeasinst.2004.11.001.

[16] Hiroki, F., Masuda, T., and Yamamoto, K., "Supersonic Fluidic Oscillator," Proceedings of the JFPS International Symposium on Fluid Power, 1989(1), pp. 345–351.

[17] Balmer, R. T., "Chapter 16 - Compressible Fluid Flow," *Modern Engineering Thermodynamics*, R.T. Balmer, ed., Academic Press, Boston, 2011, pp. 651–691.

[18] Papamoschou, D., Zill, A., and Johnson, A., "Supersonic Flow Separation in Planar Nozzles," Shock Waves, 2008, **19**(3), p. 171. https://doi.org/10.1007/s00193-008-0160-z

[19] Thompson, R. V., "Experiments Relating to Pressure Recovery in Supersonic Bistable Switches," Proceedings of the Third Cranfield Fluidics Conference, Turin, Italy, 1968, F10, p. 145.

[20] Thompson, R. V., "Supersonic Fluidics Empirical Design Data," Proceedings of the Fourth Cranfield Fluidics Conference, Coventry, England, 1970, N2, p. 17.

[21] Raghu, S., "Miniature Fluidic Devices for Flow Control," Proceedings of the ASME Fluids Engineering Division Summer Meeting, New York, N.Y., 1999.

[22] Xu, S., Martins, J.-P., and Rankin, G. W., 2017, "A Simple Hybrid Numerical Model of a Supersonic Fluidic Oscillator," Presented at the 25th Annual CFDSC Conference, Windsor, Ontario, 2017.

[23] Hiroki, F., "Fluidic Oscillator Using Supersonic Bistable Device and Its Oscillation Frequency," The Journal of Fluid Control, Vol. 21, No. 4, 1993, pp. 28–47.

[24] Rankin, Gary. W., and Xu, S., *"Unpublished Internal Report"*, 2017.

[25] "ANSYS FLUENT 12.0 User's Guide", Online Available: http://www.afs.enea.it/project/neptunius/docs/fluent/html/ug/main_pre.htm.

[26] Fujima, K., Masamura, K., and Goto, C., "Development of the 2D/3D Hybrid Model for Tsunami Numerical Simulation," Coastal Engineering Journal, Vol. 44, No. 4, 2002, pp. 373–397. https://doi.org/10.1142/S0578563402000615.

[27] McGeachy, J. D., and Chow, W. L., “A Study of Feedback Fluid Jet Oscillator with a Supersonic Power Jet: Part I: Presentation and Interpretation of the Experimental Data,” Journal of Dynamic Systems, Measurement, and Control, Vol. 95, No. 2, 1973, pp. 180–184. https://doi.org/10.1115/1.3426676.

[28] McGeachy, J. D., and Chow, W. L., “A Study of Feedback Fluid Jet Oscillator with a Supersonic Power Jet: Part II: Analytical Study of Its Characteristics,” Journal of Dynamic Systems, Measurement, and Control, Vol. 95, No. 2, 1973, pp. 185–190. https://doi.org/10.1115/1.3426677

[29] Peirone, C., and Rankin, Gary. W., “Personal Communication”, 2019.

Appendices

Appendix A

A.1. Logic for lumped parameter model to determine transient pressure change in feedback tanks

This section gives the equations and procedure used to determine the pressure change inside the feedback tank. These equations are implemented in the UDF for the lumped parameter (0D) model. The equations are derived assuming the process to be polytropic, and the mass and energy is conserved throughout the process. For any general polytropic filling/discharging process, Equation A1.1, given below, is used to determine the pressure change inside the tank.

$$\frac{d}{dt}(P)_{tank} = n * \frac{R*T_{in}}{V} * \dot{m}_{in} \qquad \text{A1.1}$$

If the filling/discharging process is isothermal, the temperature in the system will be a constant and equal to the tank fluid temperature ($T_{in} = T_{tank}$) and the polytropic index, $n = 1$. For adiabatic case, the temperature will not be constant in the system, therefore, inlet temperature is used in the equation and the polytropic index is 1.4.

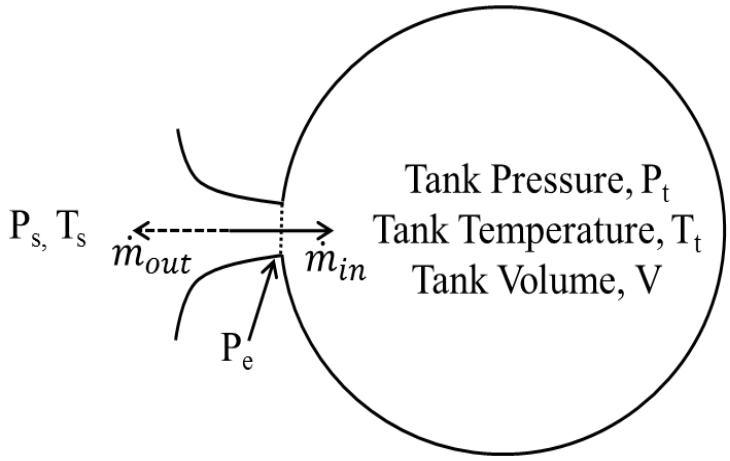

Figure A.1: Schematic diagram for tank filling analysis

The mass flow rates and mass-weighted static pressures at locations in the flow field just outside the feedback tank are monitored from the CFD solution of the flow inside the oscillator channels. Equation A1.1 is used to determine the instantaneous pressure change at each time step inside the feedback tanks. The pressures upstream and inside the tank are compared and if the total upstream pressure is larger than the tank pressure, the feedback tank is allowed to fill; otherwise, the feedback tank is full or discharging. The logic shown in Figure A.2 uses the instantaneous pressure change in one-time step to calculate the updated pressure in the next time step, thus generating the transient feedback tank pressures.

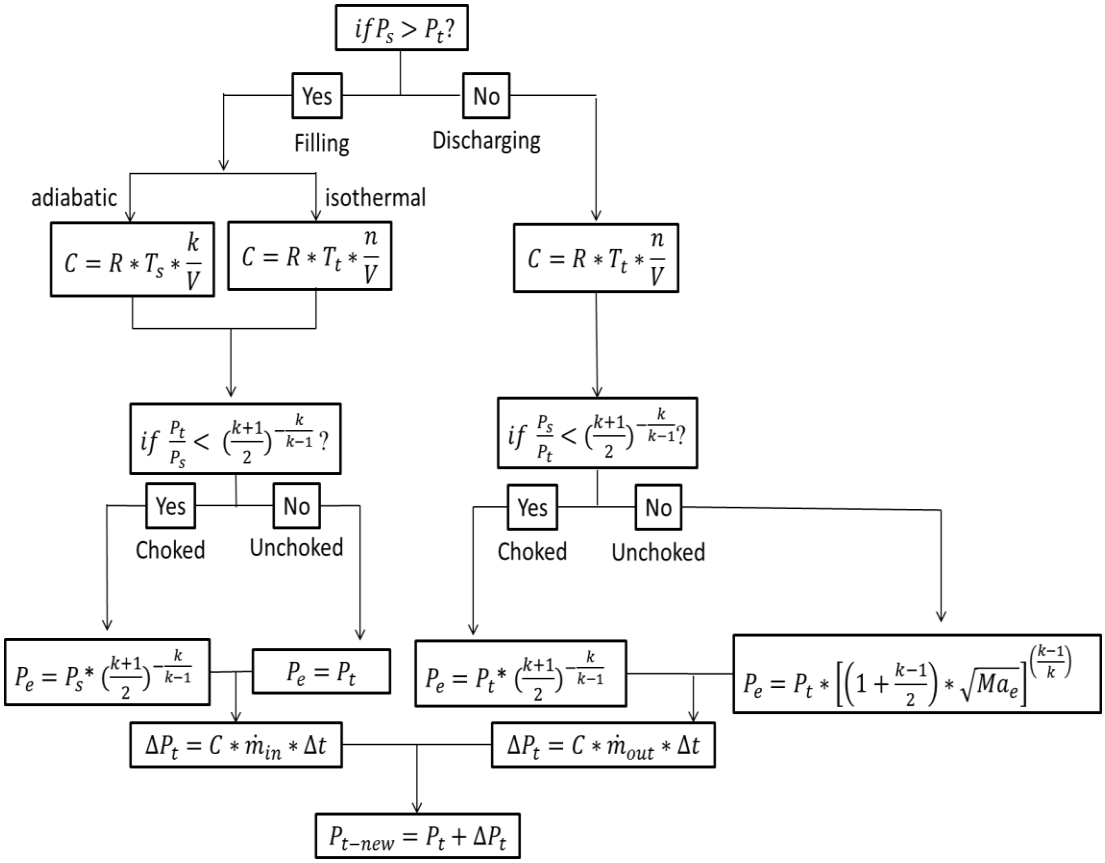

Figure A.2: Control logic of the lumped parameter model of feedback tank

A.2. Logic for lumped parameter model to determine transient pressure change in SPF chambers

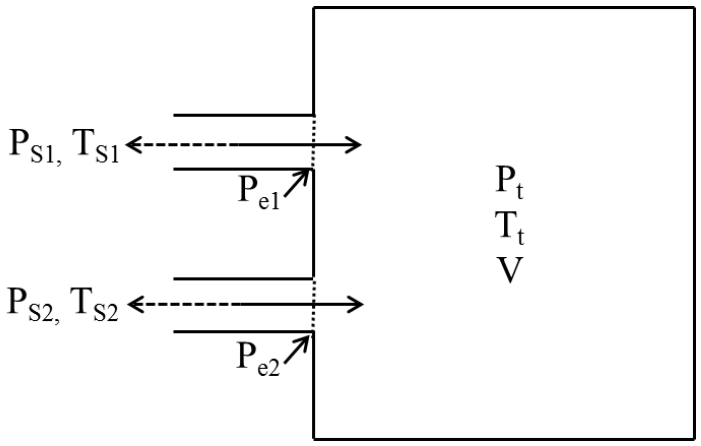

Figure A.3: Schematic diagram for tank filling analysis with two inlets

The SPF chambers are also simulated using a similar lumped parameter model as for the feedback tanks. In case of SPF chambers, the only difference is that SPF chambers have two inlets, control port inlet and exhaust port inlet, instead of one inlet as in case of feedback tanks. Equation A1.1 can be applied for each of the inlet ports. The pressures upstream of each port and inside the chamber are compared to determine whether the chamber is charging or discharging. The instant pressure change in the chamber is the summation of pressure change due to the individual ports. The logic shown in Figure A.4 uses the instantaneous pressure change in a time step to calculate the updated pressure in the next time step, thus generating the transient SPF chamber pressure.

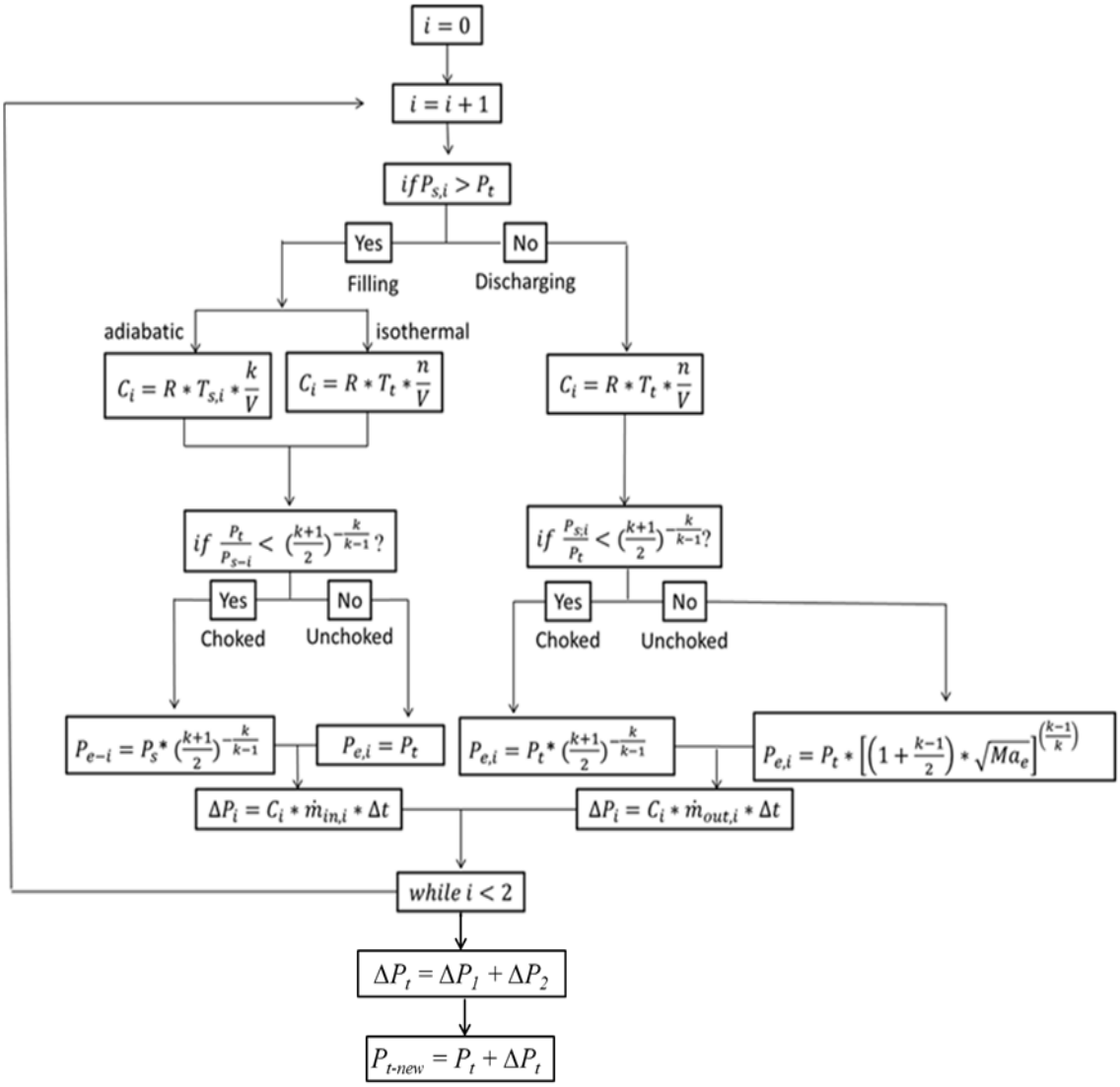

Figure A.4: Control logic of the lumped parameter model of SPF chamber

Appendix B

B.1. User Defined Function for the 2D/0D model

Within this appendix the User Defined Functions (UDFs) are explained, and then the tank filling and discharging UDF for use in the numerical model is described. ANSYS Fluent allows UDFs to be used to enhance the standard features of the solver. A UDF is written in the C programming language. Some additional macros are made available within the UDF language to simplify the functionality of the written C codes. The macros allow the code to be executed at the end of each iteration or time step, and upon exit or loading of the case. UDFs are advantageous when customized boundary conditions, property definitions, surface and volume reaction rates, and transport equations are required. The UDF can also be useful in the initialization of the model.

In this User Defined Function, the "DEFINE_PROFILE" macro is used. This macro is applied to all the boundaries of the 2D oscillator within the numerical model. This is used to define the custom boundary profile that varies as the function of time based on the calculation of pressure inside the SPF chambers and the feedback tanks. A flow chart describing the functioning of the UDF is given in Appendix A.1 and A.2. The C code used can be found in Figure D2 below.

```
/* Udf of SFO */
/* Coded By: Jean-Paul Martins & Sichang Xu, Modified by Lovepreet Singh Sidhu */

#include "udf.h"
#include "unsteady.h"

/* Global Define */

/* Global Variables Defined */
#define R 287 /* Gas Constant */
```

```
#define Ti 295 /* initial temperature*/
#define Pi 101325 /* initial pressure = 0 Pa */
#define n 1 /* Polytropic index = 1 for isothermal assumption */
#define j 1.4 /* Specific heat ratio */

/* Variables Defined for chambers */
#define PatmoI 101325 /* Atmospheric pressure outside the chamber I */
#define PatmoII 101325 /* Atmospheric pressure outside the chamber II */
#define idoI 81 /* Index of scan area for the upstream condition of chamber I */
#define idoII 80 /* Index of scan area for the upstream condition of chamber II */
#define idbcI 96 /* Index of scan line for the upstream condition of chamber I */
#define idbcII 97 /* Index of scan line for the upstream condition of chamber I */
#define VC 0.008 /* Chamber volume (m^3) */

/* Variable Define of tanks */
#define PatmI 101325 /* Atmosphere pressure outside the feedback tank I */
#define PatmII 101325 /* Atmosphere pressure outside the feedback tank II */
#define idI 75 /* Index of scan area for the upstream condition of feedback tank I */
#define idII 74 /* Index of scan area for the upstream condition of feedback tank II */
#define idtcI 94 /* Index of scan line for the upstream condition of feedback tank I */
#define idtcII 95 /* Index of scan line for the upstream condition of feedback tank II */
#define V 0.000022 /* Feedback tank volume (m^3) */

/* Variable Define of controls */
#define idcI 65 /* Index of scan area for the upstream condition of control port I */
#define idcII 64 /* Index of scan area for the upstream condition of control port II */
#define idccI 85 /* Index of scan line for the upstream condition of control port I */
#define idccII 86 /* Index of scan line for the upstream condition of control port II */

/* Variable Declaration */

/* Variable Declaration for chambers I & II */
double PsoI; /* Upstream pressure for chamber I */
double PckoI; /* Choke pressure, P_critical for chamber I */
double pboI; /* Chamber pressure I */
double PbProI; /* Critical pressure ratio for choking of Chamber I */
double TinoI; /* Inlet temperature I */
double ToI; /* Chamber temperature I */

double PsoII; /* Upstream pressure for chamber II */
double PckoII; /* Choke pressure, P_critical for chamber II */
double pboII; /* Chamber pressure II */
double PbProII; /* Critical pressure ratio for choking of Chamber II */
double TinoII; /* Inlet temperature II */
double ToII; /* Chamber temperature I */
```

```
double COI; /* Relationship between mass flow rate and pressure change at port1 */
double COII; /* Relationship between mass flow rate and pressure change at port2 */
double COIII; /* Relationship between mass flow rate and pressure change at port3 */
double COIV; /* Relationship between mass flow rate and pressure change at port4 */

double mfrOI; /* Mass flow rate at port1 */
double mfrOII; /* Mass flow rate at port2 */
double mfrOIII; /* Mass flow rate at port3 */
double mfrOIV; /* Mass flow rate at port4 */

double tt1I; /* Current time step for chamber I*/
double tt0I; /* Previous time step for chamber II */
double tt1II; /* Current time step for chamber I*/
double tt0II; /* Previous time step for chamber II */
double dPOI; /* Chamber I pressure change in current time step */
double dPOII; /* Chamber II pressure change in current time step */
double roI; /* Density in the chamber I */
double roII; /* Density in the chamber II */
double QI; /* Outlet volume flow rate for chamber I */
double QII; /* Outlet volume flow rate for chamber II */

double PbI; /* Pressure in the chamber I */
double PbII; /* Pressure in the chamber II */
double iI; /* Index of the local time step for chamber I */
double iII; /* Index of the local time step for chamber II */
double kI; /* Number of the local time step for chamber I */
double kII; /* Number of the local time step for chamber II */

FILE *champresI; /* Index of the text file to record information history for chamber I */
FILE *lastchampresI; /* Index of the text file to record information history from last time
step for chamber I */
FILE *champresII; /* Index of the text file to record information history for chamber II */
FILE *lastchampresII; /* Index of the text file to record information history from last time
step for chamber I */

/* Variable Declaration for tanks */
double PsI;  /* Upstream pressure for feedback tank I */
double PckI; /* Choke pressure, P_critical for feedback tank I */
double t1I; /* Current time step for feedback tank I */
double t0I; /* Previous time step for feedback tank I */
double CI; /* Relationship between mass flow rate and pressure change for tank I */
double mfrI; /* Mass flow rate for feedback tank I */
double ptankI; /* Pressure in the feedback tank I */
double dPI; /* Tank I pressure change in current time step */
double PbPrI; /* Critical pressure ratio for choking of tank I */
double TinI; /* Inlet temperature for tank I */
```

```
double TI; /* Temperature in tank I */
int vlvI; /* Discharge valve status for tank I */
FILE *tankpresI; /* Index of the text file to record information history for tank I */
FILE *lastpresI; /* Index of the text file to record information history from last time step
for tank I */

double PsII; /* Upstream pressure for feedback tank II */
double PckII; /* Choke pressure, P_critical for feedback tank II */
double t1II; /* Current time step for feedback tank II */
double t0II; /* Previous time step for feedback tank II */
double CII; /* Relationship between mass flow rate and pressure change for tank II */
double mfrII; /* Mass flow rate for feedback tank II */
double ptankII; /* Pressure in the feedback tank II */
double dPII; /* Tank II pressure change in current time step */
double PbPrII; /* Critical pressure ratio for choking of tank II */
double TinII; /* Inlet temperature for tank II */
double TII; /* Temperature in tank II */
int vlvII; /* Discharge valve status for tank II */
FILE *tankpresII; /* Index of the text file to record information history for tank II */
FILE *lastpresII; /* Index of the text file to record information history from last time step
for tank I */

/* Variables for control ports */
double PscI; /* Upstream pressure for control port I */
double PckcI; /* Choke pressure, P_critical for control port I */
double t1cI; /* Current time step for control port I */
double t0cI; /* Previous time step for control port I */
double CCI; /* Relationship between mass flow rate and pressure change for control I */
double mfrcI; /* Mass flow rate for control port I */
double pcontrolI; /* Pressure in the control port I */
double dPcI; /* Control port I pressure change in current time step */
double PbPrcI; /* Critical pressure ratio for choking of control port I */
double TincI; /* Inlet temperature for control port I */
double TcI; /* Temperature in control port I */

double PscII; /* Upstream pressure for control port II */
double PckcII; /* Choke pressure, P_critical for control port II */
double tc1II; /* Current time step for control port II */
double tc0II; /* Previous time step for control port II */
double CCII; /* Relationship b/w mass flow rate and pressure change for control II */
double mfrcII; /* Mass flow rate for control port II */
double pcontrolII; /* Pressure in the control port II */
double dPcII; /* Control port II pressure change in current time step */
double PbPrcII; /* Critical pressure ratio for choking of control port II */
double TincII; /* Inlet temperature for control port II */
double TcII; /* Temperature in control port II */
```

```
/* Function for Pressure at Specific Scanned Area */
double upstream_P(double idi)
{
#if !RP_HOST
Thread *t;
Domain *d;
cell_t c;

double Volume=0;
double Ps=0;
double Pop=101325; /* Operating pressure */
double Ts;
double M; /* Mach number */

d=Get_Domain(1);
t=Lookup_Thread(d,idi);

/* determining the volume average total pressure */
begin_c_loop_int(c, t)
{
Ts=C_T(c,t);
M=sqrt((SQR(C_U(c,t))+SQR(C_V(c,t)))/(j*R*Ts));
Volume+=C_VOLUME(c,t);
Ps+=pow(1+((j-1)/2)*SQR(M),(j/(j-1)))*(C_P(c,t)+Pop)*C_VOLUME(c,t);
}
end_c_loop_int(c, t)

# if RP_NODE /* Perform node synchronized actions here, does nothing in Serial */
  Ps = PRF_GRSUM1(Ps);
  Volume = PRF_GRSUM1(Volume);
# endif /* RP_NODE */

Ps=Ps/Volume;
return Ps;

# endif /* !RP_HOST */
}

/* Function for Temperature at Specific Scanned Area */
double upstream_T(double idii)
{
#if !RP_HOST
Thread *t;
Domain *d;
cell_t c;
```

```
double M; /* Mach number */
double Tin=0;
double Volume=0;
double Ts;

d=Get_Domain(1);
t=Lookup_Thread(d,idii);

/* determining the volume average temperature*/
begin_c_loop_int(c, t)
{
Ts=C_T(c,t);
M=sqrt((SQR(C_U(c,t))+SQR(C_V(c,t)))/(j*R*Ts));
Volume+=C_VOLUME(c,t);
Tin+=Ts*(1+((j-1)/2)*SQR(M))*C_VOLUME(c,t);
}
end_c_loop_int(c, t)

# if RP_NODE /* Perform node synchronized actions here, does nothing in Serial */
  Volume = PRF_GRSUM1(Volume);
  Tin = PRF_GRSUM1(Tin);
# endif /* RP_NODE */

Tin=Tin/Volume;
return Tin;

# endif /* !RP_HOST */
}

/* Function for Mass Flow Rate at Specific Scanned Area */
double massflowrate(double idiii)
{
#if !RP_HOST
Thread *t;
Domain *d;
face_t f;

double mfr=0;

d=Get_Domain(1);
t=Lookup_Thread(d,idiii);
begin_f_loop(f,t)
  if PRINCIPAL_FACE_P(f,t)
  {
  mfr+=F_FLUX(f,t);
```

```
  }
end_f_loop(f,t)

# if RP_NODE
  mfr = PRF_GRSUM1(mfr);
# endif /* RP_NODE */

mfr=mfr*0.0032;
return mfr;

#endif
}

/* Initialization */

/* Initializing parameters for chamber I */
DEFINE_INIT(initoI,d)
{
tt1I=0;
tt0I=0;
ToI=Ti;
pboI=Pi;
COI=R*(ToI)*n/VC;
ToIII=Ti;
COIII=R*(ToIII)*n/VC;
PbI=0;

node_to_host_double_4(tt1I,PbI,ToI,pboI);
#if !RP_NODE
champresI = fopen("chamber_pressureI.txt","a+");
fprintf(champresI,"%f %f %f %f\n",tt1I,PbI,ToI,pboI);
fclose(champresI);
#endif
}

/* Initializing parameters for chamber II */
DEFINE_INIT(initoII,d)
{
tt1II=0;
tt0II=0;
ToII=Ti;
pboII=Pi;
COII=R*(ToII)*n/VC;
ToIV=Ti;
COIV=R*(ToIV)*n/VC;
PbII=0;
```

```
node_to_host_double_4(tt1II,PbII,ToII,pboII);
#if !RP_NODE
champresII = fopen("chamber_pressureII.txt","a+");
fprintf(champresII,"%f %f %f %f\n",tt1II,PbII,ToII,pboII);
fclose(champresII);
#endif
}

/* Initializing parameters for tank I */
DEFINE_INIT(initI,d)
{
t1I=0;
t0I=0;
TI=Ti;
ptankI=Pi;
CI=R*TI*n/V;
vlvI=1; /* 1 is normally closed, 0 is normally open */

node_to_host_double_4(t1I,ptankI,mfrI,TI);
#if !RP_NODE
tankpresI = fopen("tankpressureI.txt","a+");
fprintf(tankpresI,"%.8f %f %.8f %f\n",t1I,ptankI,mfrI,TI);
fclose(tankpresI);
#endif
}

/* Initializing parameters for tank II */
DEFINE_INIT(initII,d)
{
t1II=0;
t0II=0;
TII=Ti;
ptankII=Pi;
CII=R*TII*n/V;
vlvII=0; /* 1 is normally closed, 0 is normally open*/

node_to_host_double_4(t1II,ptankII,mfrII,TII);
#if !RP_NODE
tankpresII = fopen("tankpressureII.txt","a+");
fprintf(tankpresII,"%.8f %f %.8f %f\n",t1II,ptankII,mfrII,TII);
fclose(tankpresII);
#endif
}

/* Initializing parameters for control ports */
```

```
DEFINE_INIT(initc,d)
{
TcI=Ti;
TcII=Ti;
CCI=R*TcI*n/VC;
CCII=R*TcII*n/VC;
CLI=0;
CLII=0;
}

/* Define Temperature Profiles */

/* Define temperature of exhaust port I */
DEFINE_PROFILE(oTI,t,nv)
{
#if !RP_HOST
face_t f;
ToI=Ti*pow((Pi/pboI),(1-n)/n);

begin_f_loop(f,t)
  if PRINCIPAL_FACE_P(f,t)
  {
  F_PROFILE(f,t,nv)=ToI;
  }
end_f_loop(f,t)
#endif
}

/* Define temperature of exhaust II */
DEFINE_PROFILE(oTII,t,nv)
{
#if !RP_HOST
face_t f;
ToII=Ti*pow((Pi/pboII),(1-n)/n);

begin_f_loop(f,t)
  if PRINCIPAL_FACE_P(f,t)
  {
  F_PROFILE(f,t,nv)=ToII;
  }
end_f_loop(f,t)
#endif
}

/*Define temperature of tank I*/
DEFINE_PROFILE(tankTI,tDTTI,nv)
```

```
{
#if !RP_HOST
face_t fDTTI;
TI=Ti*pow((Pi/ptankI),(1-n)/n);

begin_f_loop(fDTTI,tDTTI)
 if PRINCIPAL_FACE_P(fDTTI,tDTTI)
 {
 F_PROFILE(fDTTI,tDTTI,nv)=TI;
 }
end_f_loop(fDTTI,tDTTI)
#endif
}

/* Define temperature of tank II */
DEFINE_PROFILE(tankTII,t,nv)
{
#if !RP_HOST
face_t f;
TII=Ti*pow((Pi/ptankII),(1-n)/n);

begin_f_loop(f, t)
  if PRINCIPAL_FACE_P(f,t)
  {
  F_PROFILE(f,t,nv)=TII;
  }
end_f_loop(f,t)
#endif
}

/* Define temperature of control I */
DEFINE_PROFILE(cTI,t,nv)
{
#if !RP_HOST
face_t f;
TcI=Ti*pow((Pi/pboI),(1-n)/n);

begin_f_loop(f,t)
  if PRINCIPAL_FACE_P(f,t)
  {
  F_PROFILE(f,t,nv)=TcI;
  }
end_f_loop(f,t)
#endif
}
```

```
/* Define temperature of control II*/
DEFINE_PROFILE(cTII,t,nv)
{
#if !RP_HOST
face_t f;
TcII=Ti*pow((Pi/pboI),(1-n)/n);

begin_f_loop(f,t)
  if PRINCIPAL_FACE_P(f,t)
  {
  F_PROFILE(f,t,nv)=TcII;
  }
end_f_loop(f,t)
#endif
}

/* Define Pressure Profiles */

/* Define pressure of exhaust I */
DEFINE_PROFILE(opI,t,nv)
{
#if !RP_HOST
face_t f;

double MoI=0;
double AoI=0;
double areaoI[ND_ND];
PbProI=1/pow((j+1)/2,j/(j-1));
PsoI=upstream_P(idoI);
TinoI=upstream_T(idoI);

begin_f_loop(f,t)
  if PRINCIPAL_FACE_P(f,t)
  {
  F_AREA(areaoI,f,t);
  AoI+=NV_MAG(areaoI);
  MoI+=sqrt((SQR(F_U(f,t))+SQR(F_V(f,t)))/(j*R*F_T(f,t)))*NV_MAG(areaoI);
  }
end_f_loop(f,t)

# if RP_NODE
  MoI = PRF_GRSUM1(MoI)/PRF_GRSUM1(AoI);
# endif

if (pboI<PsoI)
{
```

```
        if(n==1.4)
        {
        COI=R*TinoI*n/VC;
        }
        else
        {
        COI=R*ToI*n/VC;
        }
}
else
{
COI=R*ToI*n/VC;
}

begin_f_loop(f,t)
if PRINCIPAL_FACE_P(f,t)
{
        if (pboI<PsoI) /* The tank is filling */
        {
                if((pboI/PsoI)<PbProI)
                {
                PckoI=(PsoI*PbProI);
                F_PROFILE(f,t,nv) =PckoI-PatmoI;
                }
                else
                {
                F_PROFILE(f,t,nv)=pboI-PatmoI;
                }
        }
        else /* Discharging or neutral */
        {
       if((PsoI/pboI)<PbProI)
       {
       PckoI=(pboI*PbProI);
       F_PROFILE(f,t,nv) =PckoI-PatmoI;
                }
                else
                {
                F_PROFILE(f,t,nv)=(pboI-PatmoI)*pow(1+((j-1)/2)*SQR(MoI),((j-1)/j));
                }
        }
}
end_f_loop(f,t)
#endif
}
```

```
/* Define pressure of exhaust II */
DEFINE_PROFILE(opII,t,nv)
{
#if !RP_HOST
face_t f;

double MoII=0;
double AoII=0;
double areaoII[ND_ND];
PbProII=1/pow((j+1)/2,j/(j-1));
PsoII=upstream_P(idoII);
TinoII=upstream_T(idoII);

begin_f_loop(f,t)
  if PRINCIPAL_FACE_P(f,t)
  {
  F_AREA(areaoII,f,t);
  AoII+=NV_MAG(areaoII);
  MoII+=sqrt((SQR(F_U(f,t))+SQR(F_V(f,t)))/(j*R*F_T(f,t)))*NV_MAG(areaoII);
  }
end_f_loop(f,t)

# if RP_NODE
  MoII = PRF_GRSUM1(MoII)/PRF_GRSUM1(AoII);
# endif

if (pboII<PsoII)
{
        if(n==1.4)
        {
        COII=R*TinoII*n/VC;
        }
        else
        {
        COII=R*ToII*n/VC;
        }
}
else
{
COII=R*ToII*n/VC;
}

begin_f_loop(f,t)
if PRINCIPAL_FACE_P(f,t)
{
        if (pboII<PsoII) /* The tank is filling */
```

```
        {
                if((pboII/PsoII)<PbProII)
                {
                PckoII=(PsoII*PbProII);
                F_PROFILE(f,t,nv) =PckoII-PatmoII;
                }
                else
                {
                 F_PROFILE(f,t,nv)=pboII-PatmoII;
                }
        }
        else /* Discharging or neutral */
        {
         if((PsoII/pboII)<PbProII)
        {
        PckoII=(pboII*PbProII);
        F_PROFILE(f,t,nv) =PckoII-PatmoII;
        }
        else
        {
        F_PROFILE(f,t,nv)=(pboII-PatmoII)*pow(1+((j-1)/2)*SQR(MoII),((j-1)/j));
        }
        }
}
end_f_loop(f,t)

#endif
}

/* Define pressure of tank I */
DEFINE_PROFILE(tankpI,t,nv)
{
#if !RP_HOST
face_t f;

double MI=0;
double AI=0;
double areaI[ND_ND];
PbPrI=1/pow((j+1)/2,j/(j-1));
PsI=upstream_P(idI);
TinI=upstream_T(idI);

begin_f_loop(f,t)
if PRINCIPAL_FACE_P(f,t)
  {
 F_AREA(areaI,f,t);
```

```
  AI+=NV_MAG(areaI);
  MI+=sqrt((SQR(F_U(f,t))+SQR(F_V(f,t)))/(j*R*F_T(f,t)))*NV_MAG(areaI);
  }
end_f_loop(f,t)

# if RP_NODE
  MI = PRF_GRSUM1(MI)/PRF_GRSUM1(AI);
# endif

if (ptankI<PsI)
{
        if(n==1.4)
        {
        CI=R*TinI*n/V;
        }
        else
        {
        CI=R*TI*n/V;
        }
}
else
{
CI=R*TI*n/V;
}

begin_f_loop(f,t)
  if PRINCIPAL_FACE_P(f,t)
  {
        if (ptankI<PsI) /* The tank is filling */
        {
                if((ptankI/PsI)<PbPrI)
                {
                PckI=(PsI*PbPrI);
                F_PROFILE(f,t,nv) =PckI-PatmI;
                }
                else
                {
                F_PROFILE(f,t,nv)=ptankI-PatmI;
                }
        }
        else /* Discharging or neutral */
        {
      if((PsI/ptankI)<PbPrI)
      {
      PckI=(ptankI*PbPrI);
      F_PROFILE(f,t,nv) =PckI-PatmI;
```

```
                }
                else
                {
                F_PROFILE(f,t,nv)=(ptankI-PatmI)*pow(1+((j-1)/2)*SQR(MI),((j-1)/j));
                }
        }
  }
end_f_loop(f,t)
#endif
}

/* Define pressure of tank II */
DEFINE_PROFILE(tankpII,t,nv)
{
#if !RP_HOST
face_t f;

double MII=0;
double AII=0;
double areaII[ND_ND];
PbPrII=1/pow((j+1)/2,j/(j-1));
PsII=upstream_P(idII);
TinII=upstream_T(idII);

begin_f_loop(f,t)
  if PRINCIPAL_FACE_P(f,t)
  {
  F_AREA(areaII,f,t);
  AII+=NV_MAG(areaII);
  MII+=sqrt((SQR(F_U(f,t))+SQR(F_V(f,t)))/(j*R*F_T(f,t)))*NV_MAG(areaII);
  }
end_f_loop(f,t)

# if RP_NODE
  MII = PRF_GRSUM1(MII)/PRF_GRSUM1(AII);
# endif

if (ptankII<PsII)
{
        if(n==1.4)
        {
        CII=R*TinII*n/V;
        }
        else
        {
        CII=R*TII*n/V;
```

```
        }
}
else
{
CII=R*TII*n/V;
}

begin_f_loop(f,t)
 if PRINCIPAL_FACE_P(f,t)
 {
        if (ptankII<PsII) /* The tank is filling */
        {
                if((ptankII/PsII)<PbPrII)
                {
                PckII=(PsII*PbPrII);
                F_PROFILE(f,t,nv) =PckII-PatmII;
                }
                else
                {
                F_PROFILE(f,t,nv)=ptankII-PatmII;
                }
        }
        else /* Discharging or neutral */
        {
      if((PsII/ptankII)<PbPrII)
      {
      PckII=(ptankII*PbPrII);
      F_PROFILE(f,t,nv) =PckII-PatmII;
        }
        else
        {
        F_PROFILE(f,t,nv)=(ptankII-PatmII)*pow(1+((j-1)/2)*SQR(MII),((j-1)/j));
        }
        }
 }

end_f_loop(f,t)
#endif
}

/* Define pressure of control port I */
DEFINE_PROFILE(controlpI,t,nv)
{
#if !RP_HOST
face_t f;
```

```
double McI=0;
double AcI=0;
double UCI=0;
double pressurelossI=0;
double areacI[ND_ND];
PbPrcI=1/pow((j+1)/2,j/(j-1));
PscI=upstream_P(idcI);
TincI=upstream_T(idcI);

begin_f_loop(f,t)
 if PRINCIPAL_FACE_P(f,t)
 {
 F_AREA(areacI,f,t);
 AcI+=NV_MAG(areacI);
 UCI+=sqrt((SQR(F_U(f,t))+SQR(F_V(f,t))))*NV_MAG(areacI);
 McI+=sqrt((SQR(F_U(f,t))+SQR(F_V(f,t)))/(j*R*F_T(f,t)))*NV_MAG(areacI);
 }
end_f_loop(f,t)

# if RP_NODE
 McI = PRF_GRSUM1(McI)/PRF_GRSUM1(AcI);
 UCI = PRF_GRSUM1(UCI)/PRF_GRSUM1(AcI);
# endif

if (pboI<PscI)
{
        if(n==1.4)
        {
        CCI=R*TincI*n/VC;
        }
        else
        {
        CCI=R*TcI*n/VC;
        }
}
else
{
CCI=R*TcI*n/VC;
}

begin_f_loop(f,t)
if PRINCIPAL_FACE_P(f,t)
{
        if (pboI<PscI) /* The tank is filling */
        {
                if((pboI/PscI)<PbPrcI)
```

```
                {
                PckcI=(PscI*PbPrcI);
                F_PROFILE(f,t,nv) =PckcI-PatmoI;
                }
                else
                {
                F_PROFILE(f,t,nv)=pboI-PatmoI;
                }
          }
          else /* Discharging or neutral */
          {
        if((PscI/pboI)<PbPrcI)
        {
        PckcI=(pboI*PbPrcI);
        F_PROFILE(f,t,nv) =PckcI-PatmoI;
                }
                else
                {
                F_PROFILE(f,t,nv)=(pboI-PatmoI)*pow(1+((j-1)/2)*SQR(McI),((j-1)/j));
                }
          }
}
end_f_loop(f,t)

#endif
}

/* Define pressure of control II */
DEFINE_PROFILE(controlpII,t,nv)
{
#if !RP_HOST
face_t f;

double McII=0;
double AcII=0;
double UCII=0;
double pressurelossII=0;
double areacII[ND_ND];
PbPrcII=1/pow((j+1)/2,j/(j-1));
PscII=upstream_P(idcII);
TincII=upstream_T(idcII);

begin_f_loop(f,t)
  if PRINCIPAL_FACE_P(f,t)
  {
  F_AREA(areacII,f,t);
```

```
  AcII+=NV_MAG(areacII);
  UCII+=sqrt((SQR(F_U(f,t))+SQR(F_V(f,t))))*NV_MAG(areacII);
  McII+=sqrt((SQR(F_U(f,t))+SQR(F_V(f,t)))/(j*R*F_T(f,t)))*NV_MAG(areacII);
  }
end_f_loop(f,t)

# if RP_NODE
  McII = PRF_GRSUM1(McII)/PRF_GRSUM1(AcII);
  UCII = PRF_GRSUM1(UCII)/PRF_GRSUM1(AcII);
# endif

if (pboII<PscII)
{
        if(n==1.4)
        {
        CCII=R*TincII*n/VC;
        }
        else
        {
        CCII=R*TcII*n/VC;
        }
}
else
{
CCII=R*TcII*n/VC;
}

begin_f_loop(f,t)
if PRINCIPAL_FACE_P(f,t)
{
        if (pboII<PscII) /* The tank is filling */
        {
                if((pboII/PscII)<PbPrcII)
                {
                PckcII=(PscII*PbPrcII);
                F_PROFILE(f,t,nv) =PckcII-PatmoII;
                }
                else
                {
                F_PROFILE(f,t,nv)=pboII-PatmoII;
                }
        }
        else /* Discharging or neutral */
        {
       if((PscII/pboII)<PbPrcII)
       {
```

```
        PckcII=(pboII*PbPrcII);
        F_PROFILE(f,t,nv) =PckcII-PatmoII;
          }
          else
          {
          F_PROFILE(f,t,nv)=(pboII-PatmoII)*pow(1+((j-1)/2)*SQR(McII),((j-1)/j));
          }
          }
}
end_f_loop(f,t)

#endif
}

/* Execute at end of each timestep */

/* Execute for the chamber I */
DEFINE_EXECUTE_AT_END(timeIII)
{
tt1I=CURRENT_TIME;
tt0I=PREVIOUS_TIME;

mfrOI=massflowrate(idbcI);
mfrcI=massflowrate(idccI);

kI=10000;

ToIII=Ti;
COIII=R*(ToIII)*n/VC;

for (iI=1; iI<=kI; iI++)
{
 roI=pboI/(R*ToIII);
 if (pboI>PatmoI)
 {
 QI=At*sqrt(2*(pboI-PatmoI)/roI);
 mfrOIII=alpha*QI*roI;
 }
 else
 {
 mfrOIII=0;
 }
 dPOI=(COI*mfrOI+CCI*mfrcI-COIII*mfrOIII)*(tt1I-tt0I)/kI;
 pboI=pboI+dPOI;
 }
```

```
node_to_host_double_5(tt1I,COI,CCI,CLI,pboI);
#if !RP_NODE
champresI = fopen("chamber_pressureI.txt","a+");
fprintf(champresI,"%f %f %f %f\n",tt1I,PbI,ToI,pboI);
fclose(champresI);
lastchampresI = fopen("last_chamber_pressureI.txt","w");
fprintf(lastchampresI,"%f %f %f %f\n",tt1I,PbI,ToI,pboI);
fclose(lastchampresI);

#endif
}

/* Execute for the chamber II */
DEFINE_EXECUTE_AT_END(timeIV)
{
tt1II=CURRENT_TIME;
tt0II=PREVIOUS_TIME;

mfrOII=massflowrate(idbcII);
mfrcII=massflowrate(idccII);

kII=10000;

ToIV=Ti;
COIV=R*(ToIV)*n/VC;

for (iII=1; iII<=kII; iII++)
{
 roII=pboII/(R*ToIV);
 if (pboII>PatmoI)
 {
 QII=At*sqrt(2*(pboII-PatmoI)/roII);
 mfrOIV=alpha*QII*roII;
 }
 else
 {
 mfrOIV=0;
 }
 dPOII=(COII*mfrOII+CCII*mfrcII-COIV*mfrOIV)*(tt1II-tt0II)/kII;
 pboII=pboII+dPOII;
}

node_to_host_double_5(tt1II,PbII,ToII,COIV,pboII);
#if !RP_NODE
champresII = fopen("chamber_pressureII.txt","a+");
fprintf(champresII,"%f %f %f %f\n",tt1II,PbII,ToII,pboII);
```

```
fclose(champresII);
lastchampresII = fopen("last_chamber_pressureII.txt","w");
fprintf(lastchampresII,"%f %f %f %f\n",tt1II,PbII,ToII,pboII);
fclose(lastchampresII);

#endif
}

/* Execute for tank I */
DEFINE_EXECUTE_AT_END(timeI)
{

t1I=CURRENT_TIME;
t0I=PREVIOUS_TIME;

mfrI=massflowrate(idtcI);
dPI=CI*mfrI*(t1I-t0I);

if (t1I>0)
{
if (vlvI==1)
{
ptankI=ptankI+dPI;
}
else
{
ptankI=Pi;
}

node_to_host_double_5(t1I,ptankI,mfrI,TI,PsI);
#if !RP_NODE
tankpresI = fopen("tankpressureI.txt","a+");
fprintf(tankpresI,"%.8f %f %.8f %f %f\n",t1I,ptankI,mfrI,TI,PsI);
fclose(tankpresI);
lastpresI = fopen("lastpressureI.txt","w");
fprintf(lastpresI,"%.8f %f %.8f %f %f\n",t1I,ptankI,mfrI,TI,PsI);
fclose(lastpresI);
#endif
}
else
{
node_to_host_double_5(t1I,ptankI,mfrI,TI,PsI);
#if !RP_NODE
lastpresI = fopen("lastpressureI.txt","w");
fprintf(lastpresI,"%.8f %f %.8f %f %f\n",t1I,ptankI,mfrI,TI,PsI);
fclose(lastpresI);
```

```
#endif
}
}

/* Execute for tank II */
DEFINE_EXECUTE_AT_END(timeII)
{

t1II=CURRENT_TIME;
t0II=PREVIOUS_TIME;

mfrII=massflowrate(idtcII);
dPII=CII*mfrII*(t1II-t0II);

if (t1II>0)
{
if (vlvII==1)
{
ptankII=ptankII+dPII;
}
else
{
ptankII=Pi;
}

node_to_host_double_5(t1II,ptankII,mfrII,TII,PsII);
#if !RP_NODE
tankpresII = fopen("tankpressureII.txt","a+");
fprintf(tankpresII,"%.8f %f %.8f %f %f\n",t1II,ptankII,mfrII,TII,PsII);
fclose(tankpresII);
lastpresII = fopen("lastpressureII.txt","w");
fprintf(lastpresII,"%.8f %f %.8f %f\n",t1II,ptankII,mfrII,TII);
fclose(lastpresII);
#endif
}
else
{
node_to_host_double_5(t1II,ptankII,mfrII,TII,PsII);
#if !RP_NODE
lastpresII = fopen("lastpressureII.txt","w");
fprintf(tankpresII,"%.8f %f %.8f %f\n",t1II,ptankII,mfrII,TII);
fclose(lastpresII);
#endif
}
}
```

```
/* Execute after reading data */

/* Execute after reading chamber I data */
DEFINE_EXECUTE_AFTER_DATA(after_dataIII,libudf)
{
#if !RP_NODE
lastchampresI = fopen("last_chamber_pressureI.txt","r");
fscanf(lastchampresI,"%lf %lf %lf %lf",&t1I,&PbI,&ToI,&pboI);
fclose(lastchampresI);
Message("EXECUTE_AFTER_DATAII called from %s\n",libudf);
Message("pboIII is:%f\n",pboI);
#endif

host_to_node_double_1(pboI);
}

/* Execute after reading chamber II data */
DEFINE_EXECUTE_AFTER_DATA(after_dataIV,libudf)
{
#if !RP_NODE
lastchampresII = fopen("last_chamber_pressureII.txt","r");
fscanf(lastchampresII,"%lf %lf %lf %lf",&t1II,&PbII,&ToII,&pboII);
fclose(lastchampresII);
Message("EXECUTE_AFTER_DATAII called from %s\n",libudf);
Message("pboIV is:%f\n",pboII);
#endif

host_to_node_double_1(pboII);
}

/* Execute after reading tank I data */
DEFINE_EXECUTE_AFTER_DATA(after_dataI,libudf)
{
#if !RP_NODE
lastpresI = fopen("lastpressureI.txt","r");
fscanf(lastpresI,"%lf %lf %lf %lf",&t1I,&ptankI,&mfrI,&TI);
ptankI=ptankI;
fclose(lastpresI);
Message("EXECUTE_AFTER_DATA I called from %s\n",libudf);
Message("t1I and ptankI are:%f %f\n",t1I,ptankI);
#endif

host_to_node_double_1(ptankI);
}
```

```
/* Execute after reading tank II data */
DEFINE_EXECUTE_AFTER_DATA(after_dataII,libudf)
{
#if !RP_NODE
lastpresII= fopen("lastpressureII.txt","r");
fscanf(lastpresII,"%lf %lf %lf %lf",&t1II,&ptankII,&mfrII,&TII);
ptankII=ptankII;
fclose(lastpresII);
Message("EXECUTE_AFTER_DATAII called from %s\n",libudf);
Message("t1II and ptankII are:%f %f\n",t1II,ptankII);
#endif

host_to_node_double_1(ptankII);
}

/* Define execution command */

DEFINE_ON_DEMAND(close_vlv_I)
{
vlvI=1;
}

DEFINE_ON_DEMAND(open_vlv_I)
{
vlvI=0;
}

DEFINE_ON_DEMAND(close_vlv_II)
{
vlvII=1;
}

DEFINE_ON_DEMAND(open_vlv_II)
{
vlvII=0;
}

/* END */
```

A similar UDF is used for the 2D/3D hybrid numerical model which is used to write the boundary values to a text file after every time step. These boundary values are imposed at desired boundaries and the process goes on to further time steps.

B.2. MATLAB code

A connection is established between MATLAB and Fluent so that Fluent commands are launched by the MATLAB session. A sample code for the establishing this connection can be found below in which the Fluent session is launched from MATLAB and Fluent command to run the simulation for 1 time step and 600 iterations is executed from the MATLAB.

```
clear
clc
i=0;
for i=1:10
%initialize aaS
orb=initialize_orb();
load_ansys_aas();
%connect to ANSYS products
iCoFluentUnit=actfluentserver(orb,'aaS_FluentId.txt');
%execute a Fluent TUI command
iFluentTuiInterpreter=iCoFluentUnit.getSchemeControllerInstance();
fluentResult=iFluentTuiInterpreter.doMenuCommandToString('solve/dual-time-iterate  1
600');
end
```

Vita Auctoris

NAME:	Lovepreet Singh Sidhu
PLACE OF BIRTH:	Barnala, Punjab
YEAR OF BIRTH:	1994
EDUCATION:	2013-2017, B.E. Aerospace Engineering, PEC University of Technology, Chandigarh, India
	2017-2019, M.A.Sc. Mechanical Engineering, University of Windsor, Windsor, ON, Canada